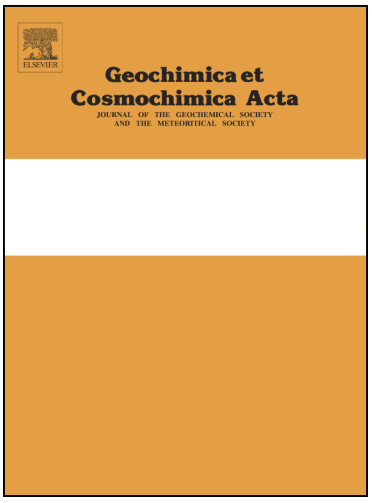

The Fe and Zn isotope composition of deep mantle source regions: Insights from Baffin Island picrites

Alex J. McCoy-West, J. Godfrey Fitton, Marie-Laure Pons, Edward C. Inglis, Helen M. Williams

PII: S0016-7037(18)30397-1
DOI: https://doi.org/10.1016/j.gca.2018.07.021
Reference: GCA 10852

To appear in: *Geochimica et Cosmochimica Acta*

Received Date: 13 March 2018
Accepted Date: 12 July 2018

Please cite this article as: McCoy-West, A.J., Godfrey Fitton, J., Pons, M-L., Inglis, E.C., Williams, H.M., The Fe and Zn isotope composition of deep mantle source regions: Insights from Baffin Island picrites, *Geochimica et Cosmochimica Acta* (2018), doi: https://doi.org/10.1016/j.gca.2018.07.021

The Fe and Zn isotope composition of deep mantle source regions: Insights from Baffin Island picrites

Alex J. McCoy-West[1, 2], J. Godfrey Fitton[3], Marie-Laure Pons[1,4], Edward C. Inglis[1,5] and Helen M. Williams[1,6]

[1]Department of Earth Sciences, Durham University, Elvet Hill, Durham DH1 3LE, UK

[2]Department of Earth, Atmosphere and Environment, Monash University, Clayton, Victoria, 3800, Australia

[3]School of GeoSciences, University of Edinburgh, Edinburgh EH9 3FE, UK

[4]Isotope Geochemistry, Department of Geosciences, University of Tübingen, Germany

[5]Institut de Physique du Globe de Paris, 1 rue Jussieu, 75238, Paris cedex 05, France

[6]Department of Earth Sciences, University of Cambridge, Downing Street, Cambridge CB2 3EQ, UK

Number of words: 8648

Number of references: 113

Number of figures: 13

Number of tables: 4

Corresponding author: Dr Alex McCoy-West (alex.mccoywest@gmail.com)

ABSTRACT

Young (61 Ma) unaltered picrites from Baffin Island, northwest Canada, possess some of the highest $^{3}He/^{4}He$ (up to 50 Ra) seen on Earth, and provide a unique opportunity to study primordial mantle that has escaped subsequent chemical modification. These high-degree partial melts also record anomalously high $^{182}W/^{184}W$ ratios, but their Sr-Nd-Hf-Pb isotopic compositons (including ^{142}Nd) are indistinguishable from those of North Atlantic mid-ocean ridge basalts. New high precision Fe and Zn stable isotope analyses of Baffin Island picrites show limited variability with $\delta^{56}Fe$ ranging from −0.03‰ to 0.13‰ and $\delta^{66}Zn$ varying from 0.18‰ to 0.28‰. However, a clear inflection is seen in both sets of isotope data around the composition of the parental melt (MgO = 21 wt %; $\delta^{56}Fe = 0.08 \pm 0.04$‰; and $\delta^{66}Zn = 0.24 \pm 0.03$‰), with two diverging trends interpreted to reflect the crystallisation of olivine and spinel in low-MgO samples and the accumulation of olivine at higher MgO. Olivine mineral separates are significantly isotopically lighter than their corresponding whole rocks ($\delta^{56}Fe \geq -0.62$‰ and $\delta^{66}Zn \geq -0.22$‰), with analyses of individual olivine phenocrysts having extremely variable Fe isotope compositions ($\delta^{56}Fe = -0.01$‰ to −0.80‰). By carrying out modelling in three-isotope space, we show that the very negative Fe isotope compositions of olivine phenocryst are the result of kinetic isotope fractionation from disequilibrium diffusional processes. An excellent correlation is observed between $\delta^{56}Fe$ and $\delta^{66}Zn$, demonstrating that Zn isotopes are fractionated by the same processes as Fe in simple systems dominated by magmatic olivine. The incompatible behaviour of Cu during magmatic evolution is consistent with the sulfide-undersaturated nature of these melts. Consequently Zn behaves as a purely lithophile element,

and estimates of the bulk Earth Zn isotope composition based on Baffin Island should therefore be robust. The ancient undegassed lower mantle sampled at Baffin Island possesses a δ^{56}Fe value that is within error of previous estimates of bulk mantle δ^{56}Fe, however, our estimate of the Baffin mantle δ^{66}Zn (0.20 ± 0.03‰) is significantly lower than some previous estimates. Comparison of our new data with those for Archean and Proterozoic komatiites is consistent with the Fe and Zn isotope composition of the mantle remaining constant from at least 3 Ga to the present day. By focusing on large-degree partial melts (e.g. komatiites and picrites) we are potenitally biasing our record to samples that will inevitably have interacted with, entrained and melted the ambient shallow mantle during ascent. For a major element such as Fe, that will continuosly participate in melting as it rises through the mantle, the final isotopic compositon of the magama will be a weighted average of the complete melting column. Thus it is unsuprising that minimal Fe isotope variation are seen between localities. In contrast, the unique geochemical signatures (e.g. He and W) displayed by the Baffin Island picrites are inferred to solely originate from the lowermost mantle and will be continuously diluted upon magma ascent.

Keywords: Iron; Zinc; Stable isotopes; picrites; komatiites; olivine; sulfide

.

1. INTRODUCTION

Accurate knowledge of the composition of the mantle helps place fundamental constraints on differentiation and evolution of the Earth. However, thus far the lack of unambiguous tracers has made identifying secular variations in mantle chemistry difficult (Canil, 2002; Hibbert et al., 2012). The Fe isotope composition of the bulk silicate Earth, based on primitive mantle xenoliths and komatiites, is well established with excellent agreement observed between different studies (Dauphas et al., 2010; Poitrasson et al., 2013; Weyer and Ionov, 2007; Williams et al., 2005). A recent data compilation has led to an estimate of δ^{56}Fe (where $\delta^{56}Fe = ((^{56}Fe/^{54}Fe_{sample}/^{56}Fe/^{54}Fe_{std}) -1) \times 1000$) of 0.033 ± 0.027 ‰ for the primitive mantle (Sossi et al., 2016b). In contrast, there have been conflicting recent estimations of the Zn isotope composition of the silicate Earth, with values of δ^{66}Zn (where $\delta^{66}Zn = ((^{66}Zn/^{64}Zn_{sample}/^{66}Zn/^{64}Zn_{std}) -1) \times 1000$) between 0.15 and 0.30 ‰ suggested (Chen et al., 2013; Doucet et al., 2016; Sossi et al., 2018; Wang et al., 2017). Initial estimates based on a basaltic average (0.28 ± 0.05‰; Chen et al., 2013) and continental mantle xenoliths (0.30 ± 0.03‰; Doucet et al., 2016) suggested a relative heavy δ^{66}Zn of the silicate Earth. However, more recent appraisals based on the depleted mid-ocean ridge basalt (MORB) mantle (0.20 ± 0.05‰; Wang et al., 2017) and ancient komatiites and peridotite data (0.16 ± 0.06‰; Sossi et al., 2018) suggest that the Earth's primitive mantle has a significantly lighter Zn isotope composition than this.

Theory predicts that under equilibrium conditions stable isotope fractionation is driven by contrasts in bonding environment and oxidation state (e.g. Polyakov, 2009; Rustad and Yin, 2009). However, the use of stable isotopes in mantle-derived rocks is further complicated

because additional variability can be generated during melt extraction, metasomatism of the mantle source, during fractional crystallisation and through changes in oxidation state (Dauphas et al., 2009; Williams et al., 2004). Thus, several studies have focused on using komatiites to place constraints on the stable Fe isotope composition of the Earth's mantle (Dauphas et al., 2010; Greber et al., 2015; Hibbert et al., 2012; Nebel et al., 2014; Sossi et al., 2018), because as the result of their large degrees of partial melting (>25%) they faithfully represent the volumetrically dominant peridotite component of the mantle; and their elevated formation temperatures (up to 1700 °C) minimise the extent of isotope fractionation upon melting (proportional to $1/T^2$). However, ancient (>2.4 Ga) komatiite samples have all been exposed to long-term surficial weathering ± serpentinisation ± variable intensities of metamorphism, all of which may perturb their original stable isotope compositions (Craddock et al., 2013; Pons et al., 2011) and the ~89Ma Gorgona komatiites studied by Hibbert et al. (2012) may sample a distinct mantle source region (Kerr, 2005; Kerr et al., 1996). Here we complement these studies by focusing on an extremely well-studied series of picrate lava flows from Baffin Island, which are considered to sample the starting head of the plume currently underneath Iceland.

The Baffin Island and the contemporaneous West Greenland picrites are virtually unaltered and represent olivine-rich magmas erupted at 61 Ma (Storey et al., 1998), and provide an excellent opportunity to study deep-seated mantle source regions. Their major element composition requires substantial amounts of partial melting (c. 25%) of an anomalously hot mantle at 1515-1560 °C (Graham et al., 1998; Herzberg et al., 2007; Larsen and Pedersen, 2000; Spice et al., 2016), which is consistent with derivation from the start-up head of the Iceland

plume. Furthermore, the primitive radiogenic isotopic compositions ($^{87}Sr/^{86}Sr$ <0.7034; εNd > +6; $^{187}Os/^{188}Os$ =0.127-0.129) and the extremely high $^{3}He/^{4}He$ ratios (up to 50 R_a) confirm the uncontaminated and undegassed nature of these melts (Dale et al., 2009; Ellam and Stuart, 2004; Kent et al., 2004; Starkey et al., 2009; Stuart et al., 2003). The Baffin Island lavas also preserve Pb and W isotope signatures that have been attributed to differentiation and isolation of a primordial region of mantle very early in Earth's history (>4.5 Gyr ago; Jackson et al., 2010; Rizo et al., 2016). Here we present new Fe and Zn stable isotope data for whole rock and olivine phenocrysts from picrites collected on the eastern margin of Baffin Island. The pristine nature of these samples allows us to precisely constrain the modern composition of Earth's lower mantle and test previous estimates of the bulk silicate Earth composition.

2. SETTING & SAMPLES

2.1. Geological setting and sample location

The North Atlantic Igneous Province comprises extensive sequences of high-Mg basalts that were erupted between 62 and 60 Ma on Baffin Island and West Greenland (along with tholeiitic lava flows preserved in south and central East Greenland, the Faeroe Islands and the British Isles) that represent the earliest phase of magmatism from the proto-Iceland plume (Saunders et al., 1997; Fig. A1). The most voluminous exposures occur in the Baffin Bay area where the magma erupted through thinned continental lithosphere in response to Paleocene rifting in the Labrador Sea and Baffin Bay (Oakey and Chalmers, 2012; Roest and Srivastava, 1989). Volcanism in Baffin Island and West Greenland is considered contemporaneous and dated at

~61 Ma (Storey et al., 1998). The volcanic rocks in West Greenland cover an onshore area of c. 22,000 km^2 (Clarke and Pedersen, 1976), and a substantially larger submerged area on the continental shelf (Chalmers et al., 1999). The overall vertical thickness of the exposed volcanic succession is 2–3 km on Disko Island and around Nuussuaq, although the total stratigraphic thickness is considerably higher due to lateral migration of the magma depocentres (Larsen and Pedersen, 2000). In the exposed onshore areas the volcanic succession can be divided into a lower part with Mg-rich olivine-phyric rocks (the Vaigat Formation) and an upper sequence of plagioclase-phyric rocks that have been assigned to several local formations. The Vaigat Formation constitutes roughly one-third of the total erupted volume. No resolvable age differences are detected, consistent with very high eruption rates, and the whole formation was probably erupted within around 0.5 Ma (Storey et al., 1998). Some members of the West Greenland magma sequence show evidence for up to 2% crustal contamination by Archean felsic basement rocks (Larsen and Pedersen, 2000; Lightfoot et al., 1997; Starkey et al., 2009), with melt inclusion data consistent with ≥10% crustal input (Yaxley et al., 2004).

The Baffin Island picrites occur as a series of sporadic outcrops along 90 km of the eastern coast of Baffin Island between Cape Searle and Cape Dyer, and on several small nearby islands in the Davis Strait (Fig. A1). The lava flows on Baffin Island are almost entirely picritic in composition and the preserved magma volumes are not large, with the lavas generally occupying depressions within the Precambrian basement. The lavas either directly overlie the Proterozoic basement or, at some locations, a thin sequence of Paleogene continental sediments intervenes between the basement and the volcanic rocks. The volcanic succession generally

consists of a lower subaqueous volcanic breccia covered by an upper sequence of usually 5-10 m thick subaerial lava flows that become thinner toward the top of each section (Clarke and Upton, 1971). The samples analyzed here were collected during a University of Edinburgh expedition in 1996, with the majority coming from continuous lava-flow sections on Padloping and Durban Islands (Lass-Evans, 2004). The volcanic rocks directly overlie the Late Paleoproterozoic basement rocks of the Hoare Bay Group (Jackson et al., 1990), the largest section on Padloping Island has a cumulative thickness of c. 750 m (Francis, 1985). The Baffin Island lavas are not distinguished stratigraphically and collectively form a coherent magmatic sequence independent of their location (Fig. 1). Sample CS-7 from Cape Searle is from a cross-cutting dyke, and not part of the main lava succession.

2.2. Petrography and chemical composition

The samples studied here have previously been characterized for their mineral compositions and whole rock major and trace element and Sr-Nd-Pb-Os-He isotope geochemistry (Lass-Evans, 2004; Dale et al., 2009; Starkey et al., 2012; Starkey et al., 2009; Stuart et al., 2003). The Baffin Island picrites are highly porphyritic rocks dominated by olivine phenocrysts with minor chromian spinel, and very rare plagioclase phenocrysts. Olivine occurs as single crystals and sometimes crystal aggregates and comprises between c. 10 and 35 modal percent of the rocks (see Table A1; Lass-Evans, 2004; Starkey, 2009). Two major olivine populations have been recognised: 1) large, near-equant crystals (~1.5-3.5 mm) that contain wide high magnesian cores ($Fo_{90–93}$ = 100 x atomic Mg/(Mg +Fe)) and thinner, normally zoned rims ($Fo_{78–85}$); and 2) small to medium-sized crystals (~ ≤1 mm) with normal zoning from $Fo_{87–88}$ in the core to $Fo_{74–85}$ at the

rim (the majority of olivine ≤0.2 mm is unzoned) (Lass-Evans, 2004; Starkey et al., 2012). The olivine phenocrysts are generally accompanied by minor (1-2%) chromian spinel up to 0.1 mm in size, one sample (DI-22) also contains plagioclase phenocrysts and glomerocrysts. Clinopyroxene has not been observed as a phenocryst phase in Baffin Island samples (this study; Clarke and Upton, 1971; Francis, 1985; Lass-Evans, 2004; Starkey, 2009). The picrites have a groundmass consisting of intergrown olivine, clinopyroxene and plagioclase microlaths, minor chromian spinel and rare glass patches.

The Baffin Island lavas analysed here have MgO contents that range from 12 to 30 wt % (n = 18) and form a cogenetic magmatic sequence, independent of their eruption locality (Fig. 1). Using the extensive major and trace element dataset presented in Starkey et al. (2009) the following trends are observed with decreasing MgO content: 1) CaO, SiO_2, Al_2O_3 and TiO_2 contents increasing in all samples; 2) relatively constant FeO and Zn abundances; 3) decreasing Ni and Cr abundances; and 4) increasing Cu, V, Y and rare earth element concentrations. On logarithmic plots of MgO content versus several incompatible element concentrations clear inflections in slope are observed around 21 wt % MgO (Fig. 2).

3. ANALYTICAL TECHNIQUES

All of the analyses described below were undertaken in the Arthur Holmes Geochemistry Laboratories at Durham University. Agate-crushed whole rock powders (50-200 mg), olivine mineral separates (c. 40 mg) or individual olivine grains (c. 0.2-9.2 mg) were digested using conventional HF-HNO_3 (2:1) Teflon beaker hotplate digestions. Some of the olivine phenocrysts

contained minute (≤0.1 mm) spinel inclusions that were intentionally left undissolved to obtain pure olivine compositions (Fig. A2), whereas an additional Parr bomb digestion step was required to completely dissolve the refractory spinels in the whole rock samples. After the samples were completely dissolved, they were evaporated to dryness and then brought into solution in 1M HCl and an aliquot containing 300 µg Fe was removed for Fe isotopic analyses (c. 5-15% of total volume) and subsequently dried and then bought into solution in 0.5 mL of 6M HCl. Iron separations were undertaken using a well-established protocol (Williams et al., 2004; 2005), which briefly comprises loading samples onto Bio-Rad Bio-Spin columns containing c. 1 mL of Bio-Rad AG1-x4 (200–400 mesh) anion exchange resin, eluting the matrix in 6M HCl and subsequently collecting the purified Fe fraction in 2M HCl. The remaining solution was then used for Zn analyses (c. 15-20 µg Zn); separations were undertaken using established procedures (Moynier et al., 2006; Pons et al., 2011), which briefly comprised a double pass through Teflon columns filled with 500 µL AG1-x4 anionic resin. Samples were loaded and the rock matrix eluted in 1.5M HBr (Zn^{2+} is strongly absorbed onto the resin in this medium) and the purified Zn fraction was then collected in 0.5M HNO_3. Column yields were checked with each batch of samples and were consistently >99%. Total procedural blanks were <50 ng for Fe and <5 ng for Zn and were negligible compared to the quantities of analyte processed.

All isotope ratio measurements were carried out on a Thermo Scientific NeptunePlus multiple-collector inductively coupled plasma mass spectrometer (MC-ICPMS) in wet plasma mode using a glass cyclonic spray chamber and a PFA 50 µl/min nebuliser. Isotope ratios are presented using conventional delta (δ = ‰) notation and are reported relative to internationally

accepted reference solutions. Iron isotope ratios are normalised relative to IRMM-014, while Zn data were bracketed using Alfa Aesar standard solution (Ponzevera et al. 2006), renormalized to JMC 3-0749 (offset = +0.27‰) commonly known as JMC-$_{Lyon}$ (Maréchal et al., 1999).

Iron isotopes were measured in medium resolution mode (a mass resolution >8000 was consistently achieved during instrument tuning) with six masses monitored during analysis (^{53}Cr, ^{54}Fe, ^{56}Fe, ^{57}Fe, ^{58}Fe and ^{60}Ni), ^{53}Cr was monitored to correct for any isobaric interference on ^{54}Fe. Sample solutions were diluted to 5-8 ppm Fe (depending on instrument sensitivity) in 0.3 M HNO_3 and measured for 50 cycles with an integration time of 4 s. Data were processed using standard– sample bracketing where the sample and standard Fe beam intensities (typically 40–45 V ^{56}Fe using a 10^{10} Ω resistor in the axial cup) were matched to within 5%. Long-term reproducibility and accuracy were evaluated by analysis of an in-house $FeCl_2$ salt standard (δ^{56}Fe = −0.722 ±0.046‰ 2s.d., n = 130) and the USGS rock standard BIR-1 (δ^{56}Fe = 0.054 ±0.039‰; 2s.d., n = 23) and are within error of previous studies (Inglis et al., 2017; Millet et al., 2012; Williams et al., 2005).

Zinc isotopes were measured in low resolution mode, with seven masses monitored during analysis (^{62}Ni, ^{63}Cu, ^{64}Zn, ^{65}Cu, ^{66}Zn, ^{67}Zn and ^{68}Zn); ^{62}Ni was monitored to correct for any isobaric interference on ^{64}Zn. Solutions were diluted to 1.5 ppm Zn in 0.5 M HNO_3 and doped with 0.5 ppm Cu to correct for mass bias fluctuations during analysis. Each analysis consisted of 50 cycles with an integration time of 4 s. We used NIST-SRM 976 for Cu doping and an exponential law to correct for mass bias fluctuations (Mason et al., 2004). A constant Zn/Cu ratio of 3:1 was used for normalising standards and unknowns to remove variations in

mass fractionation induced by variable sample matrices (Archer and Vance, 2004; Chen et al., 2009). Long-term reproducibility and accuracy were evaluated by analysis of the USGS rock standards BIR-1 (δ^{66}Zn = 0.247 ±0.030‰; 2 s.d., n = 16) and BHVO-1 (δ^{66}Zn = 0.307 ±0.016‰; 2s.d., n = 13) which are within error of previous studies (Chen et al., 2013; Sossi et al., 2015), and the JMC-Lyon solution (δ^{66}Zn = 0.009 ±0.022‰; 2 s.d., n = 19). All of the Fe and Zn isotope data presented here are mass dependent (Fig. A3); each individual analysis was checked for mass dependence prior to being included in the calculated means.

4. RESULTS

4.1. Whole rock Fe and Zn isotope data

Whole rock Fe stable isotope variations in Baffin Island picrites are limited to 0.15‰ with δ^{56}Fe ranging from −0.025‰ to 0.125‰ (Fig. 3; Table 1). As MgO content increases from 11 to 20 wt %, δ^{56}Fe values increase gradually from 0.035 ± 0.020‰ to 0.069 ± 0.015‰, with one exception sample DI-27 (MgO = 18.6 wt %) that has a significantly higher δ^{56}Fe of 0.125 ± 0.030‰. Although these values are within error of each other, a good correlation is observed between MgO and δ^{56}Fe (Fig. 3a; r^2 = 0.50). At MgO contents above 21 wt %, δ^{56}Fe displays a broad negative array against MgO (r^2 = 0.29), with δ^{56}Fe values as light as −0.025 ± 0.012‰ seen in MgO-rich samples (up to 27 wt %). The highest MgO sample PI-40 (MgO = 29.2 wt %) has a slightly heavier Fe isotopic composition, at δ^{56}Fe = 0.018 ± 0.009‰, than the other samples with MgO contents >25 wt %. The Zn stable isotopic compositions of the same rocks are even more restricted with δ^{66}Zn, varying from 0.178‰ to 0.283‰. Although more scatter is observed in

δ^{66}Zn the same general inflection point can be distinguished as for Fe isotopes. With increasing MgO contents up to 20 wt %, δ^{66}Zn values are scattered and range from 0.210 ± 0.003‰ to 0.283 ± 0.003‰. At MgO contents >21 wt % MgO, δ^{66}Zn displays a negative array with MgO (Fig. 3b; $r^2 = 0.16$) with δ^{66}Zn values as low as 0.178 ± 0.004‰ observed in some high-MgO samples. Similar inflections in Fe and Zn isotopic data are seen when they are also plotted against both compatible and incompatible trace elements (e.g. Cr and V, respectively; Fig. 4). When plotted against Cu content, Fe and Zn isotope signatures appear to behave slightly differently and become progressively heavier as Cu contents increase from 60 to 100 ppm (Fig. 4e-f), with the most evolved magma (PI-28: MgO = 11.3 wt %) having a significantly higher Cu concentration but intermediate stable isotope compositions (Cu = 121 ppm; δ^{56}Fe = 0.053 ± 0.030‰; δ^{66}Zn = 0.210 ± 0.008‰). No correlations are observed between both stable Fe and Zn isotope data and a wide range of other geochemical parameters including: 1) FeO_T or Zn contents (see Fig. A4), respectively; 2) indicators of mantle source enrichment and unique source composition (e.g. $(La/Sm)_N$ or $^3He/^4He$; Fig. 5a-b); or 3) isotopic trackers of crustal contamination including Sr-Nd-Os isotopes (Fig. 5c).

4.2. Olivine Fe and Zn isotope data

The isotopic composition of bulk olivine separates and individual crystals were investigated from three picrites with variable petrography and MgO contents (DI-24 = 24.5 wt %; DI-27 = 18.6 wt %; PI-40 =29.2 wt %). Picrites DI-24 and DI-27 are representative of the majority of Baffin Island samples; they possess a variably sized population of olivine phenocrysts up to 3 mm in length that comprise 20-25% by volume of the rock, situated in a fine-grained groundmass

consisting of plagioclase, pyroxene and olivine. Sample PI-40 contains smaller euhedral relatively equigranular olivine crystals between 0.5 and 1.2 mm in size that comprise c. 30% by volume of the rock, interspersed in a coarser matrix composed of olivine, pyroxene and plagioclase (see Fig. A5 for comparison).

The olivine fractions in picrites DI-24 and DI-27 possess significantly lighter Fe isotope compositions than their corresponding whole rocks ($\Delta^{56}Fe_{ol\text{-}WR} = \delta^{56}Fe_{ol} - \delta^{56}Fe_{WR} \sim -0.66‰$; Fig. 6), with $\delta^{56}Fe_{ol} = -0.532 \pm 0.020‰$ and $-0.616 \pm 0.023‰$, respectively (Table 2). The bulk olivine separate from sample PI-40 is significantly heavier at $\delta^{56}Fe_{ol} = -0.073 \pm 0.011‰$ and only slightly lighter ($\Delta^{56}Fe_{ol\text{-}WR} \sim -0.09‰$) than the whole rock composition. The Zn isotopic compositions of the bulk olivine separates follow a similar pattern with more negative values seen in the samples with larger olivine phenocrysts: $\delta^{66}Zn_{ol}$ in DI-24 = $-0.147 \pm 0.012‰$ and DI-27 = $-0.221 \pm 0.017‰$. Sample PI-40 has the isotopically heaviest bulk olivine separate with $\delta^{66}Zn_{Ol} = 0.037 \pm 0.024‰$. The offset between the whole rock and olivine fractions is more variable for Zn isotopes than for Fe with $\Delta^{66}Zn_{ol\text{-}WR}$ varying from −0.16‰ to −0.50‰.

Analyses of individual olivine phenocrysts were undertaken in two samples (DI-24 and PI-40), with individual grains possessing extremely variable Fe isotope compositions with $\delta^{56}Fe$ ranging from −0.011‰ to −0.797‰ (n = 14; Table 2). In sample DI-24, there is a bimodal distribution of Fe isotope compositions with four larger crystals (>1.3 mm) having very light $\delta^{56}Fe$ values from $-0.665 \pm 0.024‰$ to $-0.797 \pm 0.019‰$, another three smaller crystals and one relatively large crystal (ol8) have heavier compositions with $\delta^{56}Fe = -0.248 \pm 0.034‰$ to $-0.356 \pm 0.025‰$ (Fig. 7). In sample PI-40, all the analysed olivine crystals are <1.2 mm in length, and

they possess a more restricted and heavier range of Fe isotope compositions with δ^{56}Fe from −0.011‰ to −0.318‰ (n = 6). Similarly, a split distribution of the Fe isotope compositions is observed, with three crystals having δ^{56}Fe = −0.275 ± 0.039‰ to −0.318 ± 0.053‰, and another three at significantly heavier values with δ^{56}Fe = −0.011 ± 0.028‰ to −0.088 ± 0.033‰ similar to the bulk olivine fraction from the sample (PI-40 $\delta^{56}Fe_{ol}$ = −0.073 ± 0.011‰; Fig. 7). Two of the largest individual olivine grains in sample DI-24 were also measured for Zn isotopes. Both crystals are isotopically light relative to the whole rock, with δ^{66}Zn values of 0.045 ± 0.033‰ and −0.308 ± 0.015‰, bracketing the bulk olivine fraction in this sample (Table 2; Fig. 8b).

5. DISCUSSION

5.1. Constraining the primitive magma composition

5.1.1. The MgO content of the Baffin Island parental melt

The effects of magmatic differentiation must be accounted for before the isotopic composition of the Baffin Island mantle source can be assessed. Magnesium-rich magmas, such as komatiites and picrites, primarily differentiate through olivine crystallisation because with falling pressure during magma ascent the primary phase field of olivine expands making olivine the sole crystallising phase at atmospheric pressure to 200ºC below the liquidus (Arndt, 1976; Kinzler and Grove, 1985). The simple and predictable composition of olivine places constraints on the chemical evolution of the magmatic system and allows correction back to a parental melt composition. For picritic magmas this can be achieved using two approaches:

1) The well constrained partitioning of Fe and Mg between olivine and melt ($K_D^{Fe–Mg}$; Roeder and Emslie, 1970; Sossi and O'Neill, 2016; Toplis, 2005) may be used to calculate the Fe/Mg

ratio of the primary liquid, assuming that the most magnesian olivine observed was in equilibrium with the parental melt. The resulting Fe/Mg_{liquid} can then be converted to FeO and MgO of the melt following back calculation along the olivine control lines.

2) In high-MgO magmatic systems dominated by olivine, incompatible trace element abundances can be used to estimate the composition of the parental melt (e.g. Norman and Garcia, 1999; Rhodes, 1995). When modelling incompatible trace element concentrations, olivine accumulation can be approximated as a simple linear addition (e.g. $C_{bulk} = C_{liquid} \times f_{liquid} + C_{solid} \times f_{solid}$; where C is concentration and *f* is the proportion of each phase), whereas fractional crystallisation is an exponential process following a Rayleigh fractionation curve (i.e. $C_{liquid} = C_{original} \times F^{(D-1)}$; where F is the fraction of liquid remaining, and D is the bulk solid-liquid partition coefficient). Therefore, on a log-log plot in which compatible elements (e.g. MgO) are plotted against highly incompatible elements (where $D << 1$; e.g. Y or Yb; Fig. 2), the composition of the parental melt is given by the break in slope of the data array.

The MgO contents of Baffin Island picrites vary from 9 to 30 wt % (Starkey et al., 2009; Fig. 1), thus some of the most magnesian lavas probably contain accumulated olivine crystals. Using an olivine–liquid K_D^{Fe-Mg} of 0·33, the most forsterite-rich olivines observed [Fo_{92-93} = 100 x atomic Mg/(Mg +Fe)] are in equilibrium with melts with *mg*-number 79–81·5, which led Clarke (1970) and Francis (1985) to argue that some Baffin Bay rocks with 19–20 wt % MgO represent primary liquids. However, the observed modal proportions of Mg-rich olivine (>Fo_{90}; <1 %) in rocks with c. 20 wt % MgO are far less than the proportions expected for those melts (>10 %; Larsen and Pedersen, 2000). Furthermore, on the basis of Ni partitioning between

olivine and melt, Hart and Davis (1978) argued that rocks with >13 wt % MgO are olivine accumulative. Following a detailed petrologic study of the coeval West Greenland picrites, Larsen and Pedersen (2000) showed that the Mg-rich olivines are a fundamental part of the mineral assemblage and estimated that the parental melt had 20–21 wt % MgO on the basis of the most Fo-rich olivines. To reconcile these observations requires that the ultramafic parental melts fractionated olivine with $Fo_{86–93}$ at depth until there was 10–14 wt % MgO in the residual melt, a large proportion of the early-formed high-Mg olivines were then left at depth. Upon ascent the melts subsequently stagnated again, accumulated olivine with $Fo_{86–89}$, and were eventually erupted charged with this later-formed olivine, thus shifting the bulk compositions back to the high MgO contents observed in some samples (Larsen and Pedersen, 2000; Starkey et al., 2012). The Baffin Island lavas thus form a simple crystallisation sequence that is controlled by olivine, and so by interrogating the bulk rock compositions it is possible to establish which lavas have accumulated olivine. A small magmatic gap occurs in the Baffin Island lava sequence between 20.6 and 21.4 wt % MgO, this coincides with a clear inflection in the slope of incompatible element arrays (Fig. 2) that is observed at c. 21 wt % MgO, thus henceforth we adopt this as the composition of the Baffin Island parental melt (i.e. the original composition of the magmas from the mantle source region corrected for olivine accumulation). This estimate is in excellent agreement with previous approximations using olivine composition (e.g. Larsen and Pedersen, 2000).

5.1.2. Olivine accumulation and the Fe and Zn isotope composition of the Baffin Island parental melt

For both Fe and Zn isotopes it has previously been shown that the accumulation of olivine will shift magmas to lighter isotopic compositions due to the preferential incorporation of isotopically light Fe and Zn in this phase (Chen et al., 2013; Dauphas et al., 2010; Hibbert et al., 2012; Teng et al., 2008). The olivine fractions measured here possess Fe and Zn isotope compositions that are significantly lighter than their respective whole rocks (e.g. DI-24: $\delta^{56}Fe_{WR} = 0.05$ vs. $\delta^{56}Fe_{ol} = -0.53$ and $\delta^{66}Zn_{WR} = 0.22$ vs. $\delta^{66}Zn_{ol} = -0.15$; Fig. 6). Furthermore, the excellent correlation between the Fe and Zn isotope compositions in the Baffin Island samples ($r^2 = 0.78$; Fig. 8a), suggests that this covariance is a consequence of a single process controlling the isotope systematics. Therefore, after correcting for the obscuring effects of secondary magmatic process it is possible to determine the true Fe and Zn isotope composition of the Baffin Island melt. As olivine accumulation can be treated as a simple linear addition process, its contribution can be easily removed. For example, a significant break in slope is observed on the Cr versus MgO plot at 21 wt % MgO (Fig. 1c), which is consistent with olivine being the only accumulative phase at higher MgO contents. Thus, simply by calculating a regression line through the data for Baffin Island samples with > 21 wt % MgO, the composition of the Baffin Island parental melt can be calculated at 21 wt % MgO as $\delta^{56}Fe = 0.076 \pm 0.04‰$ and $\delta^{66}Zn = 0.242 \pm 0.03‰$ (Fig. 3). This parental melt composition can then be used to model the evolution of the Baffin Island system and compare it globally to other large-degree partial melts.

Using the calculated parental melt and the measured olivine and whole rock isotope compositions, the amount of olivine accumulation can be quantified. Due to the variable isotopic composition of the olivine populations observed in the lavas (e.g. δ^{66}Zn = 0.04 to −0.22‰; Fig. 6b), the samples with >21 wt % MgO spread out forming a mixing array with the different endmember average olivine compositions that they contain. This modelling shows that for both Fe and Zn isotopes the majority of Baffin Island lavas have <20% accumulated olivine, with a few samples containing close to 30% olivine (Fig. 6). For example, in sample PI-40 accumulation of the relatively isotopically heavy bulk olivine of this sample (δ^{56}Fe = −0.07‰; δ^{66}Zn = 0.04‰; Table 2) requires c. 30 % olivine accumulation. This estimate is in excellent agreement with those generated using major element composition and the petrography of the sample (i.e. 30% olivine phenocrysts; Fig. A5).

5.1.3. Reconciling the isotopic effects of magmatic differentiation

Fractional crystallisation can modify the stable isotope composition of an evolving melt due to differences in the bonding environment between mineral phases and liquid melt (Polyakov and Mineev, 2000; Teng et al., 2008; Weyer et al., 2005; Williams et al., 2005). With MgO content decreasing, Baffin Island samples with <21 wt % MgO, have slightly decreasing and invariant Fe and Zn isotope compositions, respectively (Fig. 3). As the measured olivine has consistently lighter δ^{56}Fe and δ^{66}Zn relative to the parental melt (Fig. 6), crystallisation and removal of pure olivine will rapidly drive the evolving melt to heavier Fe and Zn isotope compositions (Fig. 9). Therefore, to maintain the relatively invariant isotope compositions observed the fractionating

assemblage must contain an additional phase that preferentially incorporates isotopically heavy Fe and Zn. The crystallization assemblage at Baffin Island is dominated by olivine with minor chrome spinel (Francis, 1985). The presence of spinel in the fractionating assemblage is consistent with the steeper negative slope on a Cr concentration versus MgO content plot, in samples with <21 wt % MgO (Fig. 1c). While the incompatible behaviour of CaO throughout magmatic evolution (Fig. 1a) is consistent with the absence of clinopyroxene and plagioclase from the liquidus.

The proportions of phases in the crystallising assemblage may be calculated using major element systematics. Taking Baffin Island lavas with <21 wt % MgO and average mineral compositions based on Spice et al. (2016) and using a Cr_2O_3 versus MgO plot the fractioning mineral assemblage required to produce the variability seen in Baffin Island lavas consists of 98.6 % olivine and 1.4% Cr-spinel (Fig. A6). To check the validity of this fractionation assemblage trace element modelling (Cr, Ni and Sc; Fig. A7) was also undertaken with an excellent fit observed to the variability seen in Baffin Island magmas. Using this mineral modal assemblage, it is then possible to undertake Rayleigh stable isotope fractionation modelling through the differentiation sequence (samples with <21 wt % MgO). Spinel does indeed preferentially incorporate heavy Fe iron isotopes as required; based on previous measurement in Gorgona komatiites spinel-whole rock fractionation factors range from $\Delta^{56}Fe_{sp\text{-}melt}$ = 0.15-0.22 (Hibbert et al., 2012). However, due to mass balance olivine still overwhelmingly dominates the total Fe budget, (97.5% ol and 2.5% sp; calculated based on the mineralogical data in Spice et al. (2016)). To produce the best fit to the data array we have assumed a $\Delta^{56}Fe_{ol\text{-}melt}$ of 0.048 ‰

(calculated at equilibrium conditions from force constants for tholeiite and olivine at intermediate oxygen fugacity; Dauphas et al. (2014)), and used a $\Delta^{56}Fe_{sp\text{-}melt}$ of 0.22 resulting in a bulk $\Delta^{56}Fe_{mix\text{-}melt}$ of 0.052 in our preferred model (Fig. 9). This model reproduces the general concave downwards trend and variability observed in the Baffin Island lavas within the long-term error (±0.04‰). The large discrepancy between the models based on the olivine Fe isotope compositions measured herein ($\Delta^{56}Fe_{ol\text{-}melt}$ can be > −0.3; Figs. 6a and 9) and the observed whole rock compositions suggests that a disequilibrium process has affected the olivine phenocrysts.

The Zn isotope data show the same general trend as the Fe isotopes, although as the samples show significantly more variable behaviour no further modelling was undertaken. The underlying cause for the increased level of Zn isotope variability is uncertain. But this could reflect the more compatible nature of Zn in spinel relative to olivine ($D_{Zn}^{sp\text{-}melt}$ = 4.6-5.2 > $D_{Zn}^{ol\text{-}melt} \approx 1$ (Davis et al., 2013; Horn et al., 1994; Le Roux et al., 2011) which will be accompanied by a resolvable isotope fractionation, as seen between mantle spinel and olivine ($\Delta^{66}Zn_{sp\text{-}ol}$ = 0.12 ± 0.07‰; Wang et al., 2017).

5.2. Distinguishing between kinetic and equilibrium fractionation in olivine

The variable but generally very light Fe and Zn isotope compositions of olivine phenocrysts measured here (Fig. 6; $\delta^{56}Fe_{ol}$ = −0.01 to −0.79‰; $\delta^{66}Zn_{ol}$ = 0.04 to −0.22‰) may be the result of two differing magmatic processes: 1) crystallisation from an evolving melt that was initially isotopically light; or 2) diffusion of Fe between olivine and the coexisting melt.

Hypothetically, the range of $\delta^{56}Fe_{ol}$ values observed could be the result of magmatic differentiation from an initially isotopically light melt. The largest and isotopically lightest high-Fo olivine crystals (e.g. DI-24; Fig. 6) may have formed in a deep magma chamber, with the removal of these crystals driving the residual melt to heavier values (see modelling in Fig. 9; 10% fractionation of olivine of $\Delta^{56}Fe_{ol\text{-}melt} = -0.38$ will make the residue 0.04‰ heavier). After significant crystal segregation, if this melt was subsequently transported to a shallower magma chamber where the smaller and lower-Fo olivine (e.g. PI-40) formed, it would have significantly heavier isotope compositions.

However, the existence of a relationship between Fe isotope composition and crystal size (Fig. 7a), with the largest crystals containing the lightest values, suggests that some sort of disequilibrium process where the largest olivine crystals have not fully equilibrated with the melt. Previous studies using a combination of bulk digestions and modelling (Dauphas et al., 2010; Teng et al., 2011) and *in situ* analyses (Oeser et al., 2015; Sio et al., 2013) have shown that the extremely negative Fe isotope compositions of olivine crystals ($\delta^{56}Fe_{ol} \geq -1.7$‰) are the result of Fe-Mg inter-diffusion. In silicate liquids, and presumably olivine, light isotopes of an element diffuse faster than their heavier counterparts (Richter et al., 2003; Richter et al., 2009), with diffusive exchange of Fe and Mg between olivine and melt being driven by compositional gradients induced through magma mixing or magmatic differentiation. In the Baffin Island system high-forsterite olivines (up to Fo_{93}; Fig. 7b) formed in deeper magma chambers are mixed into lower Mg# melts (in equilibrium with $Fo_{86–89}$ olivine), providing an ideal environment for diffusion-based re-equilibration. The majority of olivine phenocrysts at Baffin

Island and in the coeval West Greenland picrites are normally zoned with compositional gradients towards the margins (Larsen and Pedersen, 2000; Lass-Evans, 2004; Spice et al., 2016; Starkey et al., 2012). In the absence of major element analyses for the individual crystals analysed here, we can only make inferences based on the petrographic observations and previous compositional data. A weak negative correlation is observed between average olivine forsterite contents and the δ^{56}Fe of the bulk olivine separates of the three samples investigated here (see Fig. A8), although there is significant overlap in the populations for both parameters. This correlation becomes significantly stronger ($r^2 = 0.97$) if only considering the upper quartile value of the forsterite contents for the different olivine populations. We can surmise, based on petrographic observations, that these high-Fo olivine are the largest grains (e.g. Starkey et al., 2012), and consequently as seen in Figure 7 have the lightest δ^{56}Fe, and thus we infer that crystals further from equilibrium with melt possess the most extreme δ^{56}Fe values. This scenario would be expected given that the higher the concentration gradient (i.e. further from compositional equilibrium) at a diffusional boundary the greater the rate of diffusion. Ultimately, in the absence of diffusion profiles here we must rely on the isotope data to distinguish between equilibrium and kinetic isotope fractionation processes.

To distinguish between these hypotheses it may be possible to compare the behaviour of Fe in three-isotope space because the mass-dependent fraction laws that describe isotope partitioning are different for kinetic and equilibrium reactions (Young et al., 2002). This methodology has previously been successfully applied to Mg isotopes (Olsen et al., 2013; Young

and Galy, 2004). For Fe isotopes at equilibrium conditions the fractionation factors (α) between two materials are related by the following equation:

$$\alpha^{57/54}\text{Fe} = (\alpha^{56/54}\text{Fe})^{\beta} \quad (1)$$

where the exponent β is:

$$\beta = \frac{(\frac{1}{m1} - \frac{1}{m3})}{(\frac{1}{m1} - \frac{1}{m2})} \quad (2)$$

m_1 is the atomic mass of ^{54}Fe (53.93961), m_2 is the atomic mass of ^{56}Fe (55.93494) and m_3 is the atomic mass of ^{57}Fe (56.93540). Equation 2 is the high temperature limit for the exponent under the equilibrium fractionation law. However, kinetic isotope fractionation obeys a different fractionation law (Young et al., 2002), therefore during kinetic fractionation the exponent β is instead:

$$\beta = \frac{\ln(\frac{M1}{M3})}{\ln(\frac{M1}{M2})} \quad (3)$$

where M_1, M_2, and M_3 refer to the masses in motion associated with kinetic processes. Using these equations there is a small difference in the calculated β exponent for Fe isotopes (δ^{57}Fe vs δ^{56}Fe) during equilibrium (β = 1.4750) and kinetic (β = 1.4881) mass-dependent fractionations. To facilitate comparison between the fractionation laws it is convenient to magnify the miniscule differences in β factors using Δ^{57}Fe′ notation:

$$\Delta^{57/54}\text{Fe}' = \delta^{57/54}\text{Fe}' - 1.475 \times \delta^{56/54}\text{Fe}' \quad (4)$$

where 1.475 refers to the equilibrium value for β and $\Delta^{57/54}Fe'$ is defined in terms of the linear form of δ values, δ′. The measured δ values are converted to linearized δ′ values using the following equation:

$$\delta' = 10^3 \ln\left(\frac{(\delta + 10^3)}{10^3}\right) \quad (5)$$

Values are linearized so that the calculated equilibrium β value applies for all values of $\delta^{56}Fe'$, meaning they can be plotted in three-isotope space, where equilibrium processes, by definition, will lie on a flat line. Using the non-linear form of $\delta^{56}Fe$ would cause $\Delta^{57}Fe'$ to fluctuate because of the "curvature of the fractionation relationships" in $\delta^{56}Fe - \delta^{57}Fe$ space (e.g. Young and Galy, 2004)

Conservatively, this approach can successfully (at the 2σ level) resolve kinetic versus equilibrium processes for the most fractionated samples with $\delta^{56}Fe' \leq -0.40‰$, using the median error on $\Delta^{57/54}Fe'$ determinations herein (±0.0053). For the Baffin Island olivine there is a general increase in $\Delta^{57}Fe'$ from −0.02 to 0.01 as $\delta^{56}Fe'$ becomes heavier (Fig. 10), with most of the larger olivine grains in DI-24 with light $\delta^{56}Fe$ compositions on the kinetic mass fractionation line. Taking regressions through the olivine dataset, independent of the points excluded, produces statistically resolvable slopes (Slope = 0.017−0.023 ± 0.012; Figs. 10 & A9) consistent with kinetic isotope fractionation having played a role in the formation of the Baffin Island olivine. Samples that diverge from the predicted mass fractionation laws are probably the product of a multistage history, as *in situ* isotope analyses have shown that olivines are often normally zoned with light Fe isotopes restricted to a Fe-rich region near the crystals rims, while

the cores of the crystals do not show chemical or isotopic zoning (Oeser et al., 2015; Sio et al., 2013). Therefore, even single grains will be mixtures of domains that have experienced equilibrium and kinetic mass-dependent isotope fractionations. This multistage history contributes to the variability seen in the whole-rock data with potential causes of isotopic variation including: variable proportions of melt and crystal cargo, the amount of partial melting, and the residence time of those olivine crystals at disequilibrium conditions. The fact that the generally isotopically heavier olivine in sample PI-40 falls closer to the equilibrium mass fractionation line (Fig. 10) is a consequence of these olivine forming closer to equilibrium with the melt (~Fo_{89}; Fig. 7b) later in the magmatic sequence and subsequently having less time to re-equilibrate with the melt prior to eruption. On balance the olivine data are consistent with the notion that large isotope fractionations require chemical diffusion in crystals, whereas fractional crystallization will only generate minor isotopic fractionations.

5.3. Constraints on the Baffin Island mantle source: Secular variations or lithological heterogeneity in the mantle?

5.3.1. The behaviour of sulfur in the Baffin Island melt

The onset of sulfide saturation can drastically affect the mineralogy and thus the stable isotope composition of an evolving magmatic system. Stable isotope fractionation between silicate and sulfide phases is expected due to the contrast in bonding environment (McCoy-West et al., 2017; Polyakov, 2009), with sulfide preferentially incorporating light isotopes due to their low force-constant bonds. Light Fe isotopes have been predicted for magmatic sulfides (Schuessler et al.,

2009; Williams et al., 2018) and measured in some hydrothermal sulfides (Dziony et al., 2014), but are yet to be confirmed for Zn isotopes. Iron is the most abundant transition metal, with multiple valance states and strong siderophile/chalcophile affinities, whereas Zn is monovalent (only Zn^{2+}) and a moderately chalcophile (sulfur-loving) element. However, both elements remain relatively constant in concentration throughout the development of the Baffin Island magmatic system (MgO = 7-30 wt %; Fig. 1e). It is notable that Cu, a highly chalcophile element continues to increase in concentration as MgO contents fall (Fig. 1d) because if immiscible sulfide-melt was present in the magmatic system, Cu concentrations would be expected to decrease (Fig. 11). To test the incompatible behaviour of Cu we have modelled the evolution of Cu using S-free partition coefficients (Liu et al., 2014) and the crystallisation assemblage obtained earlier (Fig. A6). When plotted against an incompatible lithophile element (e.g. Y) the model reproduces the evolution of the Baffin Island magmas well (Fig. 11). Sulfur-saturation of an evolving magma is extremely complex (Mavrogenes and O'Neill, 1999; O'Neill and Mavrogenes, 2002; Smythe et al., 2017) with the solubility of sulfur being sensitive to temperature (increases at higher temperature), pressure (increases at lower pressure) and melt composition (e.g. increases at higher FeO). Thus, the high temperature and low pressure conditions at Baffin Island (Hole, 2015; Spice et al., 2016) should promote the high solubility of S in the melt (technically a high S content at sulfide saturation) which is consistent with the incompatible behaviour of Cu. Furthermore, the excellent covariation between Fe and Zn isotopes because of magmatic processes dominated by olivine (Fig. 8) is consistent with the sulfide-undersaturated nature of the magmas and the purely lithophile behaviour of Zn at Baffin

Island. Ultimately, the absence of sulfide segregation means that estimates of the Fe or Zn isotope compositions of bulk Earth based on Baffin Island should be robust.

5.3.2. Do mineralogical variations contribute to Baffin Island's unique mantle composition?

It is well established that the source regions of some MORB and ocean island basalts (OIB) are characterised by trace element and isotopic variations that are difficult to reconcile with the melting of "normal" peridotite mantle alone (e.g. Eiler et al., 2000; Hauri, 1996; Hirschmann and Stolper, 1996; Humayun et al., 2004; Prytulak and Elliott, 2007; Sobolev et al., 2007; Williams and Bizimis, 2014). However, there is presently no consensus as to the extent or spatial distribution of these lithological heterogeneities within the mantle. The Baffin Island and West Greenland picrites possess some of the highest $^{3}He/^{4}He$ ratios so far measured from the terrestrial mantle (up to 50 Ra; Graham et al., 1998; Starkey et al., 2009; Stuart et al., 2003) and radiogenic isotopic compositions that are very similar to those in North Atlantic MORB ($^{87}Sr/^{86}Sr$ <0.7034; $\varepsilon Nd > +6$; $^{187}Os/^{188}Os$ =0.127-0.129) (Dale et al., 2009; Ellam and Stuart, 2004; Kent et al., 2004; Starkey et al., 2009). These lavas also preserve elevated $^{182}W/^{184}W$ isotope signatures consistent with an ancient component that recorded mantle-core interaction very early in Earth's history (Rizo et al., 2016), although no corresponding $^{142}Nd/^{144}Nd$ isotope anomaly, a tracer of early silicate-silicate differentiation, is observed in the same samples (de Leeuw et al., 2017). Due to the unusual characteristics of the Baffin Island mantle the possibility that lithological heterogeneities could have contributed to this unique source region must be considered.

Detecting lithological heterogeneities in the mantle relies on using the differences in elemental partitioning between the major phases in peridotite (olivine-orthopyroxene) and pyroxenite (clinopyroxene-garnet) mantle domains. Both Zn/Fe and Fe/Mn ratios have been investigated to distinguish between melting regimes (Humayun et al., 2004; Le Roux et al., 2010), on the basis that these element ratios are not significantly fractionated during melting of peridotite residues or any subsequent magmatic differentiation events. Le Roux et al. (2011) showed experimentally that during melting olivine and orthopyroxene do not significantly fractionate Mn, Fe and Zn, and because these minerals dominate the elemental budget in ultramafic systems, peridotite melts should have similar Mn/Fe and Zn/Fe as their source regions. By contrast, clinopyroxene and garnet display contrasting patterns of Zn, Mn and Fe elemental fractionation (Pertermann et al., 2004), and therefore melts of pyroxenites or eclogites would be expected to have low Mn/Fe and high Zn/Fe relative to peridotite melts. Here we have chosen to focus on the Zn/Fe ratio because it is relatively invariant during magmatic differentiation at Baffin Island ($(Zn/Fe) \times 10^4$ = 8.5-10.7; MgO = 7-29 wt %). After correction to 12 wt % MgO to allow direct comparison with other geochemical reservoirs, the $(Zn/Fe) \times 10^4$ of the Baffin Island suite is 9.69 ± 0.86; which is identical within error with estimates of MORB and the peridotite mantle (see Table 3; 9.39 ± 1.37 and 8.5 ± 2, respectively; Le Roux et al., 2010) although significantly lower than some OIB basalts with recycled components (e.g. Samoa; Fig. 12b) or the inferred composition of a pyroxenite melt ($(Zn/Fe) \times 10^4$ = 14; (Le Roux et al., 2010). Consequently, we surmise that the Baffin Island mantle source is dominated by normal peridotite mantle. This finding is unsurprising given that incorporation of recycled crustal

materials with high time-integrated Th and U abundances would be irreconcilable with the high $^{3}He/^{4}He$ signatures preserved at Baffin Island that require derivation from an unmixed and undegassed mantle source region. In contrast, a major element such as Fe is likely to participate in melting across the entire melting column and its contribution would be weighted according to where the greatest extent of melting is taking place. At Baffin Island the thinned lithosphere overlying the locus of melting would have resulted in additional melting at shallower depths and therefore "normal" Fe and Zn isotope signatures represent an integrated average of the entire melting column. Conversely, the unique geochemical signatures (e.g. He and W) displayed by the Baffin lavas are inferred to solely originate from the lowermost mantle and will be continuously diluted upon magma ascent.

5.3.3. The Zn isotope composition of the silicate Earth

Disparate estimates of the Zn isotope composition of the silicate Earth have been reported over recent years. Calculations based on basalts and continental mantle xenoliths suggest a relative heavy $\delta^{66}Zn$ of 0.28-0.30 ‰ (Chen et al., 2013; Doucet et al., 2016), whereas approximations based on the depleted MORB mantle and ancient komatiites and global peridotite data suggest that the Earth's primitive mantle has a significantly lighter Zn isotope composition at 0.16-0.20 ‰ (Sossi et al., 2018; Wang et al., 2017). The Baffin Island picrites are pristine, high degree partial melts of the mantle and thus provide an ideal suite with which to test these previous estimates. Given that Zn has a bulk partition coefficient near unity in mantle assemblages ($D_{Zn}^{mantle\text{-}melt} \approx 1$; Davis et al., 2013; Le Roux et al., 2011), during partial melting Zn is only

weakly enriched in the melt phase. However, it has been inferred and modelled that Zn isotope fractionation of up to 0.1‰ accompanies this melting (Doucet et al., 2016; Sossi et al., 2018; Wang et al., 2017). By constructing a non-modal melting model (see Table 4) we can quantify the degree of fractionation between the Baffin Island melt and its mantle source. Assuming the Baffin parental melt is the result of 25% partial melting in the garnet stability field at 1400 ºC (average temperature in Spice et al., 2016), the fractionation between the resulting melt and its complementary residue would be $\Delta^{66}Zn_{melt\text{-}mantle} = 0.042‰$ (Fig. 13b). Using the $\delta^{66}Zn$ composition of Baffin parental melt calculated previously of 0.242‰ suggests that the original mantle reservoir had a $\delta^{66}Zn$ of 0.20 ± 0.03‰, in agreement with the two lower estimates for the Zn isotope composition of the mantle (Sossi et al., 2018; Wang et al., 2017). The degree of fractionation observed in the garnet stability field model is very similar to that estimated for spinel facies melting (Sossi et al., 2018). Changing the mineral-melt partition coefficients or isotope fractionation factors has minimal effect on the modelled Zn isotope composition of the melt, with temperature being a far more sensitive parameter for driving fractionation. In summary, the Baffin Island picrites provide confirmation that the mantle has maintained a constant Zn isotope composition from at least 3.5 Ga to the present day and the $\delta^{66}Zn$ of the bulk silicate Earth is around 0.2‰ (Fig. 12b).

5.3.4. Variations in the Fe isotope composition of the mantle through time?

Determining whether the $\delta^{56}Fe$ of mantle has varied through geological time is complicated because partial melting, crystal fractionation processes and source mineralogy can all affect the

Fe isotope composition of a magma. During partial melting the more incompatible Fe^{3+} (Mallmann and O'Neill, 2009) is preferentially extracted from the residue resulting in an isotopically heavier melt. Based on the modelling presented in Dauphas et al. (2009) at ~1300ºC, assuming a primitive mantle Fe^{3+}/Fe^{2+} ratio of 0.037 (Canil et al., 1994) and 25% equilibrium melting, the degree of isotopic fractionation $\delta^{56}Fe_{melt}-\delta^{56}Fe_{source}$ is <0.04‰. Because komatiites are the results of large degrees of melting (25-40%; Sossi et al., 2016a) at elevated temperatures (>1400-1580 ºC; Nisbet et al., 1993), and both of these factors will minimise the magnitude of isotope fractionation (which is proportional to $1/T^2$), we can effectively assume that these high-degree partial melts faithfully inherit their source compositions within the current analytical errors.

As demonstrated here for Baffin Island fractional crystallisation or accumulation of olivine can significantly perturb the Fe isotope composition of a magma. Therefore, to allow direct comparisons between high-degree partial melts, the Fe isotope compositions of different komatiite suites have been corrected for magmatic differentiation/olivine accumulation to their respective primitive MgO contents (Table 3; Fig. 12a). The Baffin Island and post-3 Ga komatiites (Gorgona, Alexo and Vetreny; Dauphas et al., 2010; Hibbert et al., 2012) have $\delta^{56}Fe$ values that fall within error of estimates of the Earth's upper mantle Fe isotope composition (Weyer and Ionov, 2007). However, the pre-3 Ga komatiites (Regal and Coonterunah; Nebel et al., 2014) have resolvably lighter $\delta^{56}Fe$ values. Nebel et al. (2014) explained the light $\delta^{56}Fe$ values (corrected for olivine accumulation) of the Pilbara komatiites in terms of an early refractory reservoir formed due to previous episodes of melt extraction (i.e. Fe^{3+} is more

incompatible thus the residue of melting will be isotopically light). Alternatively, it could be speculated that the mantle became more oxidised post 3 Ga following the onset of plate tectonics and that this is reflected in a greater magnitude of mineral melt isotopic fractionation (as the latter correlates with Fe^{3+}) and hence heavier Fe isotope compositions in the melt. The Baffin Island picrites possess a "primitive" and relatively undegassed source (unradiogenic lithophile isotopes and high $^{3}He/^{4}He$) that has "normal" $\delta^{56}Fe$ and $\delta^{66}Zn$, whereas if the Regal and Coonterunah komatiites sampled a source that had already experienced melt extraction (thus light $\delta^{56}Fe$) this would presumably be degassed in terms of noble gases (unfortunately this cannot be tested for such old samples). Further evidence that the Baffin Island source has not experienced any previous melt extraction/degassing events within the first ~ 500 Myr of Earth history comes from the absence of $^{142}Nd/^{144}Nd$ anomalies (de Leeuw et al., 2017). Future ^{142}Nd analyses of the Pilbara komatiites may be able to confirm the existence of a previous Hadean melting event, as has been observed for some Archean komatiites (Puchtel et al., 2016; Touboul et al., 2012), which would enable this scenario to be tested. To resolve this conundrum further, detailed analyses of the Fe isotope composition of mantle melts through space and time will also be required.

6. CONCLUSIONS

The Baffin Island picrites represent an unusual mantle endmember that has undergone limited degassing and preserves primitive radiogenic isotope signatures. Here we present Fe and Zn stable isotope compositions of these unaltered picrites and demonstrate that:

1) Using the inflection method, the Baffin Island parental melt is considered to contain 21 wt % MgO. After correction for the effects of magmatic differentiation the Baffin Island parental melt has a δ^{56}Fe of 0.08 ± 0.04‰ and δ^{66}Zn of 0.24 ± 0.03‰.
2) The incompatible nature of Cu and an excellent covariation between Fe and Zn isotopes, consistent with Zn behaving as a lithophile element, attest to the sulfide-undersaturated nature of the Baffin Island samples during the whole magmatic sequence.
3) On the basis of Zn/Fe ratios the Baffin Island mantle source is considered to be composed entirely of normal peridotite mantle. This is what would be expected for the preservation of extremely elevated ^{3}He/^{4}He signatures and primordial radiogenic isotope signatures.
4) By undertaking three-isotope-space modelling we have shown that the very negative Fe-isotope ratios of olivine phenocryst ($\delta^{56}Fe_{ol} = -0.8$‰), are the result of kinetic isotope fractionation from disequilibrium diffusional processes.
5) After correcting for the effect of partial melting, the Zn isotope composition of the Baffin Island mantle source is δ^{66}Zn = 0.20 ± 0.03‰ consistent with some recent similar estimates of the composition of the bulk mantle (Sossi et al., 2018; Wang et al., 2017).
6) Although the Baffin Island picrites sample a primordial and undegassed source region they are entirely unremarkable in their Fe and Zn isotope compositions. These magmas are consistent with both the Fe and Zn isotope ratios of the mantle being constant from at least 3 Ga to the present day.

Acknowledgements

Geoff Nowell, in particular is thanked for his generous help and insightful discussions over the last few years. AMW is grateful to Kevin Burton for the time to complete this work and Marc-Alban Millet and Paolo Sossi and for discussions and insights on stable isotopes. The rock samples were collected in 1996 by Ian Snape, Coleen Cole and Sally Brown during an Edinburgh University expedition to Baffin Island supported by a grant from the Laidlaw-Hall Trust. Corliss Kin I Sio, Adriana Heimann and an anonymous reviewer are thanked for are thanked for their constructive comments. This project was funded by the European Research Council (ERC Starting Grant 306655 "HabitablePlanet") and a NERC Consortium Grant (NE/M0003/1 "Deep Volatiles") to HMW.

REFERENCES

An, Y., Huang, J.-X., Griffin, W.L., Liu, C. and Huang, F. (2017) Isotopic composition of Mg and Fe in garnet peridotites from the Kaapvaal and Siberian cratons. Geochimica et Cosmochimica Acta 200, 167-185.
Archer, C. and Vance, D. (2004) Mass discrimination correction in multiple-collector plasma source mass spectrometry: an example using Cu and Zn isotopes. Journal of Analytical Atomic Spectrometry 19, 656-665.
Arndt, N.T. (1976) Melting relations of ultramafic lavas (komatiites) at 1 atm and high pressure. Carnegie Institution of Washington Yearbook 75, 555-562.
Canil, D. (2002) Vanadium in peridotites, mantle redox and tectonic environments: Archean to present. Earth and Planetary Science Letters 195, 75-90.
Canil, D., O'Neill, H.S.C., Pearson, D.G., Rudnick, R.L., McDonough, W.F. and Carswell, D.A. (1994) Ferric iron in peridotites and mantle oxidation states. Earth and Planetary Science Letters 123, 205-220.
Chalmers, J.A., Pulvertaft, T.C.R., Marcussen, C. and Pedersen, A.K. (1999) New insight into the structure of the Nuussuaq Basin, central West Greenland. Marine and Petroleum Geology 16, 197-224.
Chen, H., Savage, P.S., Teng, F.-Z., Helz, R.T. and Moynier, F. (2013) Zinc isotope fractionation during magmatic differentiation and the isotopic composition of the bulk Earth. Earth and Planetary Science Letters 369, 34-42.
Chen, J.-B., Louvat, P., Gaillardet, J. and Birck, J.-L. (2009) Direct separation of Zn from dilute aqueous solutions for isotope composition determination using multi-collector ICP-MS. Chemical Geology 259, 120-130.
Clarke, D.B. (1970) Tertiary basalts of Baffin Bay: Possible primary magma from the mantle. Contributions to Mineralogy and Petrology 25, 203-224.
Clarke, D.B. and Pedersen, A.K. (1976) Tertiary volcanic province of West Greenland, in: Escher, A., Watt, W.S. (Eds.), Geology of Greenland. Geological Survey of Greenland, Copenhagen, pp. 364-385.
Clarke, D.B. and Upton, B.G.J. (1971) Tertiary Basalts of Baffin Island: Field Relations and Tectonic Setting. Canadian Journal of Earth Sciences 8, 248-258.
Craddock, P.R., Warren, J.M. and Dauphas, N. (2013) Abyssal peridotites reveal the near-chondritic Fe isotopic composition of the Earth. Earth and Planetary Science Letters 365, 63-76.
Dale, C.W., Pearson, D.G., Starkey, N.A., Stuart, F.M., Ellam, R.M., Larsen, L.M., Fitton, J.G. and Macpherson, C.G. (2009) Osmium isotopes in Baffin Island and West Greenland picrites: Implications for the 187Os/188Os composition of the convecting mantle and the nature of high 3He/4He mantle. Earth and Planetary Science Letters 278, 267-277.
Dauphas, N., Craddock, P.R., Asimow, P.D., Bennett, V.C., Nutman, A.P. and Ohnenstetter, D. (2009) Iron isotopes may reveal the redox conditions of mantle melting from Archean to Present. Earth and Planetary Science Letters 288, 255-267.
Dauphas, N., Roskosz, M., Alp, E.E., Neuville, D.R., Hu, M.Y., Sio, C.K., Tissot, F.L.H., Zhao, J., Tissandier, L., Médard, E. and Cordier, C. (2014) Magma redox and structural controls on iron isotope variations in Earth's mantle and crust. Earth and Planetary Science Letters 398, 127-140.
Dauphas, N., Teng, F.-Z. and Arndt, N.T. (2010) Magnesium and iron isotopes in 2.7 Ga Alexo komatiites: Mantle signatures, no evidence for Soret diffusion, and identification of diffusive transport in zoned olivine. Geochimica et Cosmochimica Acta 74, 3274-3291.
Davis, F.A., Humayun, M., Hirschmann, M.M. and Cooper, R.S. (2013) Experimentally determined mineral/melt partitioning of first-row transition elements (FRTE) during partial melting of peridotite at 3GPa. Geochimica et Cosmochimica Acta 104, 232-260.
de Leeuw, G.A.M., Ellam, R.M., Stuart, F.M. and Carlson, R.W. (2017) 142Nd/144Nd inferences on the nature and origin of the source of high 3He/4He magmas. Earth and Planetary Science Letters 472, 62-68.
Doucet, L.S., Mattielli, N., Ionov, D.A., Debouge, W. and Golovin, A.V. (2016) Zn isotopic heterogeneity in the mantle: A melting control? Earth and Planetary Science Letters 451, 232-240.
Dziony, W., Horn, I., Lattard, D., Koepke, J., Steinhoefel, G., Schuessler, J.A. and Holtz, F. (2014) In-situ Fe isotope ratio determination in Fe–Ti oxides and sulfides from drilled gabbros and basalt from the IODP Hole 1256D in the eastern equatorial Pacific. Chemical Geology 363, 101-113.

Eiler, J.M., Schiano, P., Kitchen, N. and Stolper, E.M. (2000) Oxygen-isotope evidence for recycled crust in the sources of mid-ocean-ridge basalts. Nature 403, 530.
Ellam, R.M. and Stuart, F.M. (2004) Coherent He–Nd–Sr isotope trends in high $^{3}He/^{4}He$ basalts: Implications for a common reservoir, mantle heterogeneity and convection. Earth and Planetary Science Letters 228, 511-523.
Francis, D. (1985) The Baffin Bay lavas and the value of picrites as analogues of primary magmas. Contributions to Mineralogy and Petrology 89, 144-154.
Graham, D.W. (2002) Noble gases in MORB and OIB: Observational constraints for the characterization of mantle source reservoirs. Reviews in Mineralogy and Geochemistry 46, 247-318.
Graham, D.W., Larsen, L.M., Hanan, B.B., Storey, M., Pedersen, A.K. and Lupton, J.E. (1998) Helium isotope composition of the early Iceland mantle plume inferred from the Tertiary picrites of West Greenland. Earth and Planetary Science Letters 160, 241-255.
Greber, N.D., Puchtel, I.S., Nägler, T.F. and Mezger, K. (2015) Komatiites constrain molybdenum isotope composition of the Earth's mantle. Earth and Planetary Science Letters 421, 129-138.
Hart, S.R. and Davis, K.E. (1978) Nickel partitioning between olivine and silicate melt. Earth and Planetary Science Letters 40, 203-219.
Hauri, E.H. (1996) Major-element variability in the Hawaiian mantle plume. Nature 382, 415-419.
Herzberg, C., Asimow, P.D., Arndt, N., Niu, Y., Lesher, C.M., Fitton, J.G., Cheadle, M.J. and Saunders, A.D. (2007) Temperatures in ambient mantle and plumes: Constraints from basalts, picrites, and komatiites. Geochemistry, Geophysics, Geosystems 8, Q02006.
Hibbert, K.E.J., Williams, H.M., Kerr, A.C. and Puchtel, I.S. (2012) Iron isotopes in ancient and modern komatiites: Evidence in support of an oxidised mantle from Archean to present. Earth and Planetary Science Letters 321–322, 198-207.
Hirschmann, M.M. and Stolper, E.M. (1996) A possible role for garnet pyroxenite in the origin of the “garnet signature” in MORB. Contributions to Mineralogy and Petrology 124, 185-208.
Hole, M.J. (2015) The generation of continental flood basalts by decompression melting of internally heated mantle. Geology 43, 311-314.
Horn, I., Foley, S.F., Jackson, S.E. and Jenner, G.A. (1994) Experimentally determined partitioning of high field strength- and selected transition elements between spinel and basaltic melt. Chemical Geology 117, 193-218.
Humayun, M., Qin, L. and Norman, M.D. (2004) Geochemical Evidence for Excess Iron in the Mantle Beneath Hawaii. Science 306, 91.
Inglis, E.C., Debret, B., Burton, K.W., Millet, M.-A., Pons, M.-L., Dale, C.W., Bouilhol, P., Cooper, M., Nowell, G.M., McCoy-West, A.J. and Williams, H.M. (2017) The behavior of iron and zinc stable isotopes accompanying the subduction of mafic oceanic crust: A case study from Western Alpine ophiolites. Geochemistry, Geophysics, Geosystems 18, 2562-2579.
Jackson, G.D., Hunt, P.A., Loveridge, W.D. and Parrish, R.R. (1990) Reconnaissance geochronology of Baffin Island, N.W.T. , Radiogenic age and isotopic studies: Report 3. Geological Survey of Canada, pp. 123-148.
Jackson, M.G., Carlson, R.W., Kurz, M.D., Kempton, P.D., Francis, D. and Blusztajn, J. (2010) Evidence for the survival of the oldest terrestrial mantle reservoir. Nature 466, 853.
Kent, A.J.R., Stolper, E.M., Francis, D., Woodhead, J., Frei, R. and Eiler, J. (2004) Mantle heterogeneity during the formation of the North Atlantic Igneous Province: Constraints from trace element and Sr-Nd-Os-O isotope systematics of Baffin Island picrites. Geochemistry, Geophysics, Geosystems 5, Q11004.
Kerr, A.C. (2005) La Isla de Gorgona, Colombia: A petrological enigma? Lithos 84, 77-101.
Kerr, A.C., Marriner, G.F., Arndt, N.T., Tarney, J., Nivia, A., Saunders, A.D. and Duncan, R.A. (1996) The petrogenesis of Gorgona komatiites, picrites and basalts: new field, petrographic and geochemical constraints. Lithos 37, 245-260.
Kinzler, R.J. and Grove, T.L. (1985) Crystallization and differentiation of Archean komatiite lavas from northeast Ontario: Phase equilibrium and kinetic studies. American Mineralogist 70, 40-51.

Konter, J.G., Pietruszka, A.J., Hanan, B.B., Finlayson, V.A., Craddock, P.R., Jackson, M.G. and Dauphas, N. (2016) Unusual δ56Fe values in Samoan rejuvenated lavas generated in the mantle. Earth and Planetary Science Letters 450, 221-232.
Larsen, L.M. and Pedersen, A.K. (2000) Processes in high-Mg, high-T magmas: Evidence from olivine, chromite and glass in Palaeogene picrites from West Greenland. Journal of Petrology 41, 1071-1098.
Lass-Evans, S. (2004) The anatomy of the ancestral Iceland plume: A chemical and isotopic study of the tertiary basalts and picrites from Baffin Island, School of Geosciences. Ph.D. thesis, University of Edinburgh, Edinburgh, Scotland, p. 265.
Le Roux, V., Dasgupta, R. and Lee, C.T.A. (2011) Mineralogical heterogeneities in the Earth's mantle: Constraints from Mn, Co, Ni and Zn partitioning during partial melting. Earth and Planetary Science Letters 307, 395-408.
Le Roux, V., Lee, C.T.A. and Turner, S.J. (2010) Zn/Fe systematics in mafic and ultramafic systems: Implications for detecting major element heterogeneities in the Earth's mantle. Geochimica et Cosmochimica Acta 74, 2779-2796.
Lightfoot, P.C., Hawkesworth, C.J., Olshefsky, K., Green, T., Doherty, W. and Keays, R.R. (1997) Geochemistry of Tertiary tholeiites and picrites from Qeqertarssuaq (Disko Island) and Nuussuaq, West Greenland with implications for the mineral potential of comagmatic intrusions. Contributions to Mineralogy and Petrology 128, 139-163.
Liu, X., Xiong, X., Audétat, A., Li, Y., Song, M., Li, L., Sun, W. and Ding, X. (2014) Partitioning of copper between olivine, orthopyroxene, clinopyroxene, spinel, garnet and silicate melts at upper mantle conditions. Geochimica et Cosmochimica Acta 125, 1-22.
Ludwig, K.R. (2008) Isoplot 3.71, 3.71 ed. Berkeley Geochronology Centre.
Mallmann, G. and O'Neill, H.S.C. (2009) The crystal/melt partitioning of V during mantle melting as a function of oxygen fugacity compared with some other elements (Al, P, Ca, Sc, Ti, Cr, Fe, Ga, Y, Zr and Nb). Journal of Petrology 50, 1765-1794.
Maréchal, C.N., Télouk, P. and Albarède, F. (1999) Precise analysis of copper and zinc isotopic compositions by plasma-source mass spectrometry. Chemical Geology 156, 251-273.
Mason, T.F.D., Weiss, D.J., Horstwood, M., Parrish, R.R., Russell, S.S., Mullane, E. and Coles, B.J. (2004) High-precision Cu and Zn isotope analysis by plasma source mass spectrometry Part 2. Correcting for mass discrimination effects. Journal of Analytical Atomic Spectrometry 19, 218-226.
Mavrogenes, J.A. and O'Neill, H.S.C. (1999) The relative effects of pressure, temperature and oxygen fugacity on the solubility of sulfide in mafic magmas. Geochimica et Cosmochimica Acta 63, 1173-1180.
McCoy-West, A.J., Millet, M.-A. and Burton, K.W. (2017) The neodymium stable isotope composition of the silicate Earth and chondrites. Earth and Planetary Science Letters 480, 121-132.
Millet, M.-A., Baker, J.A. and Payne, C.E. (2012) Ultra-precise stable Fe isotope measurements by high resolution multiple-collector inductively coupled plasma mass spectrometry with a 57Fe–58Fe double spike. Chemical Geology 304–305, 18-25.
Moynier, F., Albarède, F. and Herzog, G.F. (2006) Isotopic composition of zinc, copper, and iron in lunar samples. Geochimica et Cosmochimica Acta 70, 6103-6117.
Nebel, O., Campbell, I.H., Sossi, P.A. and Van Kranendonk, M.J. (2014) Hafnium and iron isotopes in early Archean komatiites record a plume-driven convection cycle in the Hadean Earth. Earth and Planetary Science Letters 397, 111-120.
Nisbet, E.G., Cheadle, M.J., Arndt, N.T. and Bickle, M.J. (1993) Constraining the potential temperature of the Archaean mantle: A review of the evidence from komatiites. Lithos 30, 291-307.
Norman, M.D. and Garcia, M.O. (1999) Primitive magmas and source characteristics of the Hawaiian plume: Petrology and geochemistry of shield picrites. Earth and Planetary Science Letters 168, 27-44.
O'Neill, H.S.C. and Mavrogenes, J.A. (2002) The sulfide capacity and the sulfur content at sulfide saturation of silicate melts at 1400°C and 1 bar. Journal of Petrology 43, 1049-1087.
Oakey, G.N. and Chalmers, J.A. (2012) A new model for the Paleogene motion of Greenland relative to North America: Plate reconstructions of the Davis Strait and Nares Strait regions between Canada and Greenland. Journal of Geophysical Research 117.

Oeser, M., Dohmen, R., Horn, I., Schuth, S. and Weyer, S. (2015) Processes and time scales of magmatic evolution as revealed by Fe–Mg chemical and isotopic zoning in natural olivines. Geochimica et Cosmochimica Acta 154, 130-150.
Olsen, M., B. , Schiller, M., Krot, A.N. and Bizzarro, M. (2013) Magnesium Isotope Evidence for Single Stage Formation of CB Chondrules by Colliding Planetesimals. The Astrophysical Journal Letters 776, L1.
Palme, H. and O'Neill, H.S.C. (2014) 3.1 - Cosmochemical estimates of mantle composition, in: Holland, H.D., Turekian, K.K. (Eds.), Treatise on Geochemistry (Second Edition). Elsevier, Oxford, pp. 1-39.
Pedersen, A.K. (1979) Basaltic glass with high-temperature equilibrated immiscible sulphide bodies with native iron from disko, central West Greenland. Contributions to Mineralogy and Petrology 69, 397-407.
Pertermann, M., Hirschmann, M.M., Hametner, K., Günther, D. and Schmidt, M.W. (2004) Experimental determination of trace element partitioning between garnet and silica-rich liquid during anhydrous partial melting of MORB-like eclogite. Geochemistry, Geophysics, Geosystems 5, Q05A01.
Poitrasson, F., Delpech, G. and Grégoire, M. (2013) On the iron isotope heterogeneity of lithospheric mantle xenoliths: implications for mantle metasomatism, the origin of basalts and the iron isotope composition of the Earth. Contributions to Mineralogy and Petrology 165, 1243-1258.
Polyakov, V.B. (2009) Equilibrium iron isotope fractionation at core-mantle boundary conditions. Science 323, 912-914.
Polyakov, V.B. and Mineev, S.D. (2000) The use of Mössbauer spectroscopy in stable isotope geochemistry. Geochimica et Cosmochimica Acta 64, 849-865.
Pons, M.-L., Quitté, G., Fujii, T., Rosing, M.T., Reynard, B., Moynier, F., Douchet, C. and Albarède, F. (2011) Early Archean serpentine mud volcanoes at Isua, Greenland, as a niche for early life. Proceedings of the National Academy of Sciences 108, 17639-17643.
Prytulak, J. and Elliott, T. (2007) TiO2 enrichment in ocean island basalts. Earth and Planetary Science Letters 263, 388-403.
Puchtel, I.S., Blichert-Toft, J., Touboul, M., Horan, M.F. and Walker, R.J. (2016) The coupled 182W-142Nd record of early terrestrial mantle differentiation. Geochemistry, Geophysics, Geosystems 17, 2168-2193.
Puchtel, I.S., Hofmann, A.W., Mezger, K., Shchipansky, A.A., Kulikov, V.S. and Kulikova, V.V. (1996) Petrology of a 2.41 Ga remarkably fresh komatiitic basalt lava lake in Lion Hills, central Vetreny Belt, Baltic Shield. Contributions to Mineralogy and Petrology 124, 273-290.
Rajamani, V. and Naldrett, A.J. (1978) Partitioning of Fe, Co, Ni, and Cu between sulfide liquid and basaltic melts and the composition of Ni-Cu sulfide deposits. Economic Geology 73, 82-93.
Rhodes, J.M. (1995) The 1852 and 1868 Mauna Loa picrite eruptions: Clues to parental magma compositions and the magmatic plumbing system, in: Rhodes, J.M., Lockwood, J.P. (Eds.), Mauna Loa Revealed: Structure, composition, history, and hazards. AGU, Geophisical Monograph, pp. 241-265.
Richter, F.M., Davis, A.M., DePaolo, D.J. and Watson, E.B. (2003) Isotope fractionation by chemical diffusion between molten basalt and rhyolite. Geochimica et Cosmochimica Acta 67, 3905-3923.
Richter, F.M., Watson, E.B., Mendybaev, R., Dauphas, N., Georg, B., Watkins, J. and Valley, J. (2009) Isotopic fractionation of the major elements of molten basalt by chemical and thermal diffusion. Geochimica et Cosmochimica Acta 73, 4250-4263.
Rizo, H., Walker, R.J., Carlson, R.W., Horan, M.F., Mukhopadhyay, S., Manthos, V., Francis, D. and Jackson, M.G. (2016) Preservation of Earth-forming events in the tungsten isotopic composition of modern flood basalts. Science 352, 809.
Roeder, P.L. and Emslie, R.F. (1970) Olivine-liquid equilibrium. Contributions to Mineralogy and Petrology 29, 275-289.
Roest, W.R. and Srivastava, S.P. (1989) Sea-floor spreading in the Labrador Sea: A new reconstruction. Geology 17, 1000-1003.
Rustad, J.R. and Yin, Q.-Z. (2009) Iron isotope fractionation in the Earth/'s lower mantle. Nature Geosci 2, 514-518.
Saunders, A.D., Fitton, J.G., Norry, M.J. and Kent, R.W. (1997) The North Atlantic Igneous Province, in: Mahoney, J.J., Coffin, M.F. (Eds.), Large Igneous Provinces. American Geophysical Union Monograph, pp. 45–93.

Schuessler, J.A., Schoenberg, R. and Sigmarsson, O. (2009) Iron and lithium isotope systematics of the Hekla volcano, Iceland — Evidence for Fe isotope fractionation during magma differentiation. Chemical Geology 258, 78-91.
Sio, C.K.I., Dauphas, N., Teng, F.-Z., Chaussidon, M., Helz, R.T. and Roskosz, M. (2013) Discerning crystal growth from diffusion profiles in zoned olivine by in situ Mg–Fe isotopic analyses. Geochimica et Cosmochimica Acta 123, 302-321.
Smythe, D.J., Wood, B.J. and Kiseeva, E.S. (2017) The S content of silicate melts at sulfide saturation: New experiments and a model incorporating the effects of sulfide composition. American Mineralogist 102, 795-803.
Sobolev, A.V., Hofmann, A.W., Kuzmin, D.V., Yaxley, G.M., Arndt, N.T., Chung, S.L., Danyushevsky, L.V., Elliott, T., Frey, F.A., Garcia, M.O., Gurenko, A.A., Kamenetsky, V.S., Kerr, A.C., Krivolutskaya, N.A., Matvienkov, V.V., Nikogosian, I.K., Rocholl, A., Sigurdsson, I.A., Sushchevskaya, N.M. and Teklay, M. (2007) The amount of recycled crust in sources of mantle-derived melts. Science 316, 412-417.
Sossi, P.A., Eggins, S.M., Nesbitt, R.W., Nebel, O., Hergt, J.M., Campbell, I.H., O'Neill, H.S.C., Van Kranendonk, M. and Davies, D.R. (2016a) Petrogenesis and Geochemistry of Archean Komatiites. Journal of Petrology 57, 147-184.
Sossi, P.A., Halverson, G.P., Nebel, O. and Eggins, S.M. (2015) Combined Separation of Cu, Fe and Zn from Rock Matrices and Improved Analytical Protocols for Stable Isotope Determination. Geostandards and Geoanalytical Research 39, 129-149.
Sossi, P.A., Nebel, O. and Foden, J. (2016b) Iron isotope systematics in planetary reservoirs. Earth and Planetary Science Letters 452, 295-308.
Sossi, P.A., Nebel, O., O'Neill, H.S.C. and Moynier, F. (2018) Zinc isotope composition of the Earth and its behaviour during planetary accretion. Chemical Geology 477, 73-84.
Sossi, P.A. and O'Neill, H.S.C. (2016) Liquidus temperatures of komatiites and the effect of cooling rate on element partitioning between olivine and komatiitic melt. Contributions to Mineralogy and Petrology 171, 49.
Spice, H.E., Fitton, J.G. and Kirstein, L.A. (2016) Temperature fluctuation of the Iceland mantle plume through time. Geochemistry, Geophysics, Geosystems 17, 243-254.
Starkey, N.A. (2009) Evolution of the Earth's mantle-crust-atmosphere system from the trace element and isotope geochemistry of the plume-mantle reservoir, School of Geosciences. Ph.D. thesis, University of Edinburgh, Edinburgh, Scotland, p. 232.
Starkey, N.A., Fitton, J.G., Stuart, F.M. and Larsen, L.M. (2012) Melt inclusions in olivines from early Iceland plume picrites support high 3He/4He in both enriched and depleted mantle. Chemical Geology 306–307, 54-62.
Starkey, N.A., Stuart, F.M., Ellam, R.M., Fitton, J.G., Basu, S. and Larsen, L.M. (2009) Helium isotopes in early Iceland plume picrites: Constraints on the composition of high 3He/4He mantle. Earth and Planetary Science Letters 277, 91-100.
Storey, M., Duncan, R.A., Pedersen, A.K., Larsen, L.M. and Larsen, H.C. (1998) 40Ar/39Ar geochronology of the West Greenland Tertiary volcanic province. Earth and Planetary Science Letters 160, 569-586.
Stuart, F.M., Lass-Evans, S., Fitton, J.G. and Ellam, R.M. (2003) High 3He/4He ratios in picritic basalts from Baffin Island and the role of a mixed reservoir in mantle plumes. Nature 424, 57-59.
Teng, F.-Z., Dauphas, N. and Helz, R.T. (2008) Iron Isotope Fractionation During Magmatic Differentiation in Kilauea Iki Lava Lake. Science 320, 1620-1622.
Teng, F.-Z., Dauphas, N., Helz, R.T., Gao, S. and Huang, S. (2011) Diffusion-driven magnesium and iron isotope fractionation in Hawaiian olivine. Earth and Planetary Science Letters 308, 317-324.
Teng, F.-Z., Dauphas, N., Huang, S. and Marty, B. (2013) Iron isotopic systematics of oceanic basalts. Geochimica et Cosmochimica Acta 107, 12-26.
Toplis, M.J. (2005) The thermodynamics of iron and magnesium partitioning between olivine and liquid: criteria for assessing and predicting equilibrium in natural and experimental systems. Contributions to Mineralogy and Petrology 149, 22-39.
Touboul, M., Puchtel, I.S. and Walker, R.J. (2012) ^{182}W evidence for long-term preservation of early mantle differentiation products. Science 335, 1065.

Walter, M.J. (1998) Melting of garnet peridotite and the origin of komatiite and depleted lithosphere. Journal of Petrology 39, 29-60.
Wang, Z.-Z., Liu, S.-A., Liu, J., Huang, J., Xiao, Y., Chu, Z.-Y., Zhao, X.-M. and Tang, L. (2017) Zinc isotope fractionation during mantle melting and constraints on the Zn isotope composition of Earth's upper mantle. Geochimica et Cosmochimica Acta 198, 151-167.
Weyer, S., Anbar, A.D., Brey, G.P., Münker, C., Mezger, K. and Woodland, A.B. (2005) Iron isotope fractionation during planetary differentiation. Earth and Planetary Science Letters 240, 251-264.
Weyer, S. and Ionov, D.A. (2007) Partial melting and melt percolation in the mantle: The message from Fe isotopes. Earth and Planetary Science Letters 259, 119-133.
Williams, H.M. and Bizimis, M. (2014) Iron isotope tracing of mantle heterogeneity within the source regions of oceanic basalts. Earth and Planetary Science Letters 404, 396-407.
Williams, H.M., McCammon, C.A., Peslier, A.H., Halliday, A.N., Teutsch, N., Levasseur, S. and Burg, J.-P. (2004) Iron Isotope Fractionation and the Oxygen Fugacity of the Mantle. Science 304, 1656-1659.
Williams, H.M., Peslier, A.H., McCammon, C., Halliday, A.N., Levasseur, S., Teutsch, N. and Burg, J.P. (2005) Systematic iron isotope variations in mantle rocks and minerals: The effects of partial melting and oxygen fugacity. Earth and Planetary Science Letters 235, 435-452.
Williams, H.M., Prytulak, J., Woodhead, J.D., Kelley, K.A., Brounce, M. and Plank, T. (2018) Interplay of crystal fractionation, sulfide saturation and oxygen fugacity on the iron isotope composition of arc lavas: An example from the Marianas. Geochimica et Cosmochimica Acta 226, 224-243.
Yaxley, G.M., Kamenetsky, V.S., Kamenetsky, M., Norman, M.D. and Francis, D. (2004) Origins of compositional heterogeneity in olivine-hosted melt inclusions from the Baffin Island picrites. Contributions to Mineralogy and Petrology 148, 426-442.
Young, E.D. and Galy, A. (2004) The Isotope Geochemistry and Cosmochemistry of Magnesium. Reviews in Mineralogy and Geochemistry 55, 197-230.
Young, E.D., Galy, A. and Nagahara, H. (2002) Kinetic and equilibrium mass-dependent isotope fractionation laws in nature and their geochemical and cosmochemical significance. Geochimica et Cosmochimica Acta 66, 1095-1104.

Figure Captions

Figure 1: Variation of selected major and trace elements versus MgO content in Baffin Island picrites. Whole rock data (n = 94) are from Starkey et al. (2009). Samples are distinguished based on their MgO content, with samples with >21 wt % MgO having accumulated olivine crystals and samples with <21 wt % MgO having undergone crystal fractionation. Samples analyzed in this study (circles) are distinguished based on location.

Figure 2: The variation of Y (a) and Yb (b) versus MgO plotted on a logarithmic scale. The break in slope of the magmatic evolution line of a suite is considered to mark the parental magma composition. Whole rock data are from Starkey et al. (2009).

Figure 3: Whole rock variations of $\delta^{56}Fe$ (a) and $\delta^{66}Zn$ (b) versus the MgO content of Baffin Island samples. Separate regression lines are plotted through the samples with >21 and <21 wt % MgO. Two sample are excluded because they are mineralogically distinct; PI-40 due to its lack of large inherited olivine phenocrysts like those observed in the other olivine-accumulative samples; and DI-27 because of the abundant large olivine phenocrysts not seen in other samples with <21 wt % MgO (see Table A1 for complete descriptions). Regression lines and error envelopes (shaded area) are calculated using Isoplot (Ludwig, 2008) using the long-term analytical errors and assuming a Model 2 fit (which assigns equal weight avoiding the mistake of weighting the points according to analytical errors). The regression lines from the samples with >21 wt % MgO are used to calculate the parental isotopic composition of the Baffin Island melt

at 21 wt % MgO. Throughout this paper error bars on individual points are the 95% s.e. on that sample, with the error on the parental melt composition taken as the long-term 2 s.d. on the basaltic reference standard BIR-1 ($\delta^{56}Fe = \pm 0.04‰$; $\delta^{66}Zn = \pm 0.03‰$). MgO contents are from Starkey et al. (2009). The weak correlation probabilities in samples with >21 wt % MgO are the result of the slightly stochastic nature of olivine accumulation in these samples, because the olivines are variably isotopically heterogeneous due to diffusional processes (see text for further discussion).

Figure 4: Whole rock variations of $\delta^{56}Fe$ and $\delta^{66}Zn$ versus the Cr (a-b), V (c-d) and Cu (e-f) concentrations of Baffin Island samples. The parental melt composition is calculated at 21 wt % based on a regression through the samples with >21 wt % MgO as shown in Figure 2.Trace element data are from Starkey et al. (2009).

Figure 5: Whole rock variations in $\delta^{56}Fe$ versus La/Sm_N, $^{87}Sr/^{86}Sr$ and $^{3}He/^{4}He$, respectively. (a) Elemental values are from Starkey et al. (2009) and are normalized to CI chondrite values (Palme and O'Neill, 2014). (b) Comparative data for West Greenland (Lightfoot et al., 1997) show the limited extent of crustal contamination in the Baffin Island suite. An additional 14 of 53 analysed West Greenland lavas plot off the graph with $^{87}Sr/^{86}Sr$ values up to 0.7122 observed. (c) The measured $^{3}He/^{4}He$ of all other Baffin Island and West Greenland lavas are shown for comparison (Starkey et al., 2009; Stuart et al., 2003). An estimate for MORB is also plotted ($^{3}He/^{4}He = 8 \pm 1$ and $\delta^{56}Fe = 0.105 \pm 0.04$ ‰ (Graham, 2002; Teng et al., 2013).

Figure 6: Comparison of whole rock and olivine mineral separate δ^{56}Fe (a) and δ^{66}Zn (b) isotope data. Larger symbols are bulk olivine analyses (c. 40 mg), with smaller symbols representing individual phenocrysts (0.2-9.2 mg). Best-fit lines are drawn through the composition of the parental melt (see Fig. 2), the whole rock composition and that of the bulk olivine separate. The numbers indicate the amount (wt. %) of olivine accumulated. MgO contents are from Starkey et al. (2009) and (Lass-Evans, 2004).

Figure 7: (a) Iron isotopic composition of individual olivine phenocrysts versus crystal size. Larger symbols are bulk (multi-grain) olivine analyses. The size of the bulk fraction is based on the average of the individual crystals, or for DI-27 the description in Lass-Evans (2004). Grain ol8 in sample DI-24 appears to be an outlier with a large size and relatively heavy δ^{56}Fe (further discussion later). (b) Box and whisker plot of the forsterite composition (Fo = molar ((Mg/ (Mg + Fe)) * 100) of olivine cores from the studied Baffin Island samples using data are from Lass-Evans (2004). Compositional data are not available for PI-40 so data from PI-41 are used instead: both samples come from the chilled margins of adjacent lava flows, and have similar sized olivine, olivine proportions and bulk rock compositions. Published data for Baffin Island olivines (n = 246; 17 lava flows) are from Starkey et al. (2012) and Spice et al. (2016).

Figure 8: The correlation of δ^{56}Fe and δ^{66}Zn in simple magmatic systems controlled by olivine crystallisation. (a) Whole rock Baffin Island and Kilauea Iki lava lake samples; and (b) with the

addition of olivine separates from Baffin Island. Regression lines and error envelopes (shaded area) were calculated using Isoplot (Ludwig, 2008). Kilauea Iki lava lake data come from Teng et al. (2008) and Chen et al. (2013).

Figure 9: Rayleigh fractionation model of the $\delta^{56}Fe$ evolution of Baffin Island lavas as fractional crystallization proceeds. Modelling starts from the parental melt where $\delta^{56}Fe = 0.076‰$. Two olivine-only models (diamonds) are presented with $\Delta^{56}Fe_{ol\text{-}melt}$ of −0.38 and −0.15 representing the median olivine ($\delta^{56}Fe_{ol} = -0.31‰$) composition measured here, and average PI-40 olivine ($\delta^{56}Fe_{ol} = -0.07‰$), respectively. A single spinel only (circles) crystallization model with $\Delta^{56}Fe_{sp\text{-}melt}$ of 0.22 is shown. A mixed assemblage model (squares) comprising 98.6% olivine, and 1.4% spinel reproduces all of the data points within long-term error (± 0.04‰; the shaded field). This model assumes a $\Delta^{56}Fe_{ol\text{-}melt} = 0.048‰$ (equilibrium value calculated from Dauphas et al. (2014) and $\Delta^{56}Fe_{sp\text{-}melt} = 0.22‰$ (Hibbert et al., 2012). The mixed assemblage and proportion of crystallization in the Baffin Island lavas is calculated based on MgO and Cr_2O_3 systematics (see Fig. A6).

Figure 10: Resolving mechanisms of isotope fractionation using a three-isotope diagram. Baffin Island olivine and whole rock data are plotted relative to the predicted equilibrium ($\beta = 1.4750$; Slope = 0) and kinetic ($\beta = 1.4881$; Slope = 0.0267) mass fractionation laws. The symbols representing the olivine crystals are scaled relative to the individual crystals size. Bulk olivine fractions are represented with a cross. Regression line and error envelope (shaded area) is

calculated through the olivine data using Isoplot (Ludwig, 2008). Data points are plotted with long-term error on $\delta^{56/54}Fe'$ (±0.039) and the median error on $\Delta^{57/54}Fe'$ (±0.0053) unless the measured errors are larger (errors where propagated as described in Young and Galy (2004). The two points that fall furthest from the correlation line (uncoloured symbols) have been excluded from the regression. However, independent of the points included the regression produces a non-zero slope consistent with kinetic isotope fractionation having affected the olivines (see Figure A9). Grain ol8 in sample DI-24 does not fit the broad correlation between $\delta^{56}Fe$ and crystal size seen in the other grains (Fig. 7) and falls significantly outside error of the predicted mass fractionation lines, thus it is not considered a good representation of the major processes we are attempting to understand.

Figure 11: Determining the effect of S using trace element modelling to examine the fractionating assemblage in the Baffin Island lavas with <21 wt % MgO. Trace element data are from Starkey et al. (2009). The silicate only (squares) fractionating assemblage assumes 98.6% olivine and 1.4% spinel (see Figs. A6 and A7) and uses partition coefficients from Liu et al. (2014) and Mallmann and O'Neill (2009). A second model (triangles) shows the effect 0.5% sulfide being removed with the fractionating silicate assemblage using a D_{Cu} sulfide-melt of 380 taken from picrite lavas (Pedersen, 1979). The pure sulfide model (crosses) shows the result of efficient removal sulfide melt assuming a lower estimate of D_{Cu} sulfide-melt of 180 (Rajamani and Naldrett, 1978). The composition of the parental melt is determined using the inflection

method (Y = 16.1 ppm; Cu = 91.5 ppm). For the silicate models the symbols represent 5% crystallization increments, whereas in the sulfide only system they represent 0.1% increments.

Figure 12: (a) The Fe isotope composition of selected mantle melts with time. All data have been corrected for magmatic differentiation using regressions to the primitive MgO content of the respective melt (Dauphas et al., 2010; Hibbert et al., 2012; Nebel et al., 2014). Fertile upper mantle composition (Weyer and Ionov, 2007) and selected ocean island basalt data (Konter et al., 2016; Teng et al., 2013) also shown. (b) The Zn/Fe (x 10^4) ratios of mantle melts calculated at 12 wt% MgO against time. Data are from a compilation presented in Le Roux et al. (2010) or calculated herein see Table 3.

Figure 13: (a) The change in δ^{66}Zn as a function of MgO of a range of rock types. Data plotted include Baffin Island picrites and rock standards (this paper), unmetasomatised peridotites (Sossi et al., 2018; Wang et al., 2017), mid ocean ridge basalts (Wang et al., 2017) and ocean island basalts (Chen et al., 2013; Wang et al., 2017), and spinifex-texture basalts and komatiites (Sossi et al., 2018). Two disparate estimates of bulk silicate Earth composition from Chen et al. (2013) and Sossi et al. (2018) are also shown. (b) The variation in δ^{66}Zn relative to Zn concentration in mantle-derived melts. Two non-modal fractional melting models with residues (filled) and melts (hollow symbols) are shown: the spinel facies model, ranging from 0.5-30% melting in 10% increments, comes directly from Sossi et al. (2018) and assumes an initial δ^{66}Zn of 0.16‰ and

melting at 1300ºC; the garnet facies model, ranging from 0.5-30% melting in 5% increments, derived herein (Table 4), assumes an initial δ^{66}Zn of 0.2‰ and melting at 1400ºC.

Table Footnotes

Table 1

() Numbers in parentheses represent a separate digestion. *n* is the number of replicate analyses on the mass spectrometer. Every sample was measured during multiple analytical sessions. To represent measurement uncertainty both the two-standard deviation (2 s.d.) and 95% standard errors (95% s.e. =*t* x s.d./$(n)^{1/2}$, where *t* = inverse survival function of the Student's t-test at the 95% significance level and (*n* −1) degrees of freedom) are presented. MgO and Cu data is from Starkey et al. (2009).

Table 2

a) Individual unbroken olivine grains were hand-picked and photographed using a binocular microscope (Fig. A2), sizes were measured digitally and represent the maximum length in the long dimension. Other parameters as in Table 1.

Table 3

a) MgO contents are the parental melt compositions reported (Dauphas et al., 2010; Nebel et al., 2014; Puchtel et al., 1996; Sossi et al., 2016a) or where missing calculated herein using the inflection method. (b) Fe isotope data for Komatiites (Dauphas et al., 2010; Hibbert et al., 2012; Nebel et al., 2014) have been corrected for magmatic differentiation to their primitive MgO contents using linear interpolation. Ocean island basalt data as also corrected to primitive melt compositions (Konter et al., 2016; Teng et al., 2013). c) To simplify comparison Zn/Fe ratios are predicted at 12 wt% MgO based on regression line equations (i.e. Le Roux et al., 2010). Due to the near unity of D_{Zn} in olivine large amounts of olivine accumulation have no significant effect on Zn/Fe ratios. Errors herein have been calculated conservatively using 2 standard deviations on Zn/Fe ratios of samples with 10-14 wt% MgO or have been assumed to be 1.2 where insufficient data is available. No Zn concentration data was found for the Alexo samples. d) Peridotite mantle values come from Sossi et al. (2016b) and Le Roux et al. (2011).

Table 4

a) Melting assemblage from (Walter, 1998); b) Partition coefficients from Davis et al. (2013); c) Olivine-orthopyroxene-clinopyroxene isotope fractionation factors are taken from Sossi et al. (2018); garnet

Figure 1

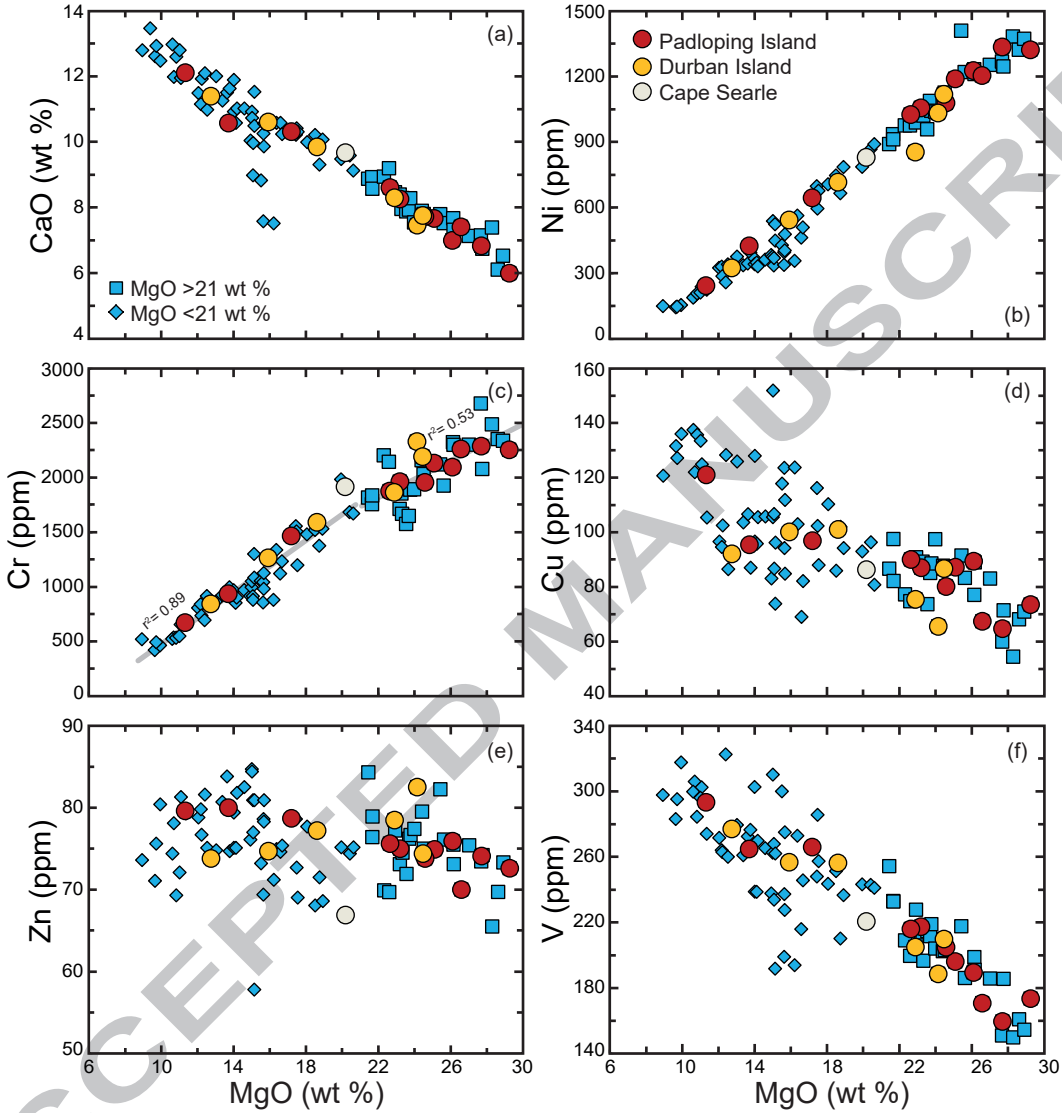

Figure 2

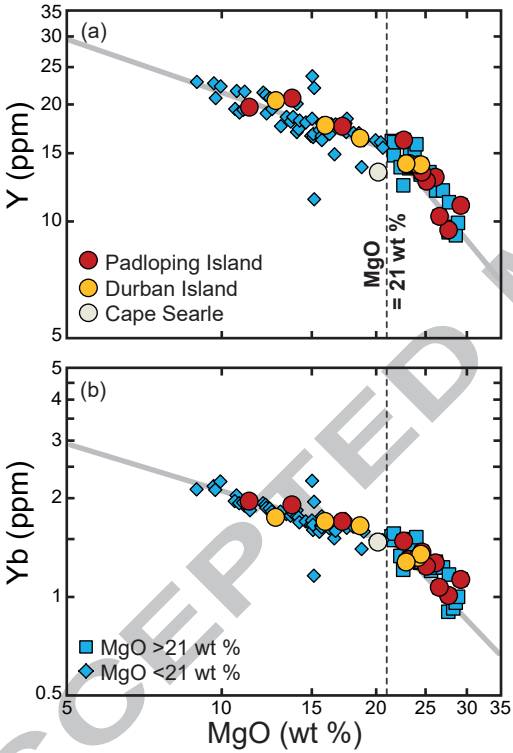

Figure 3

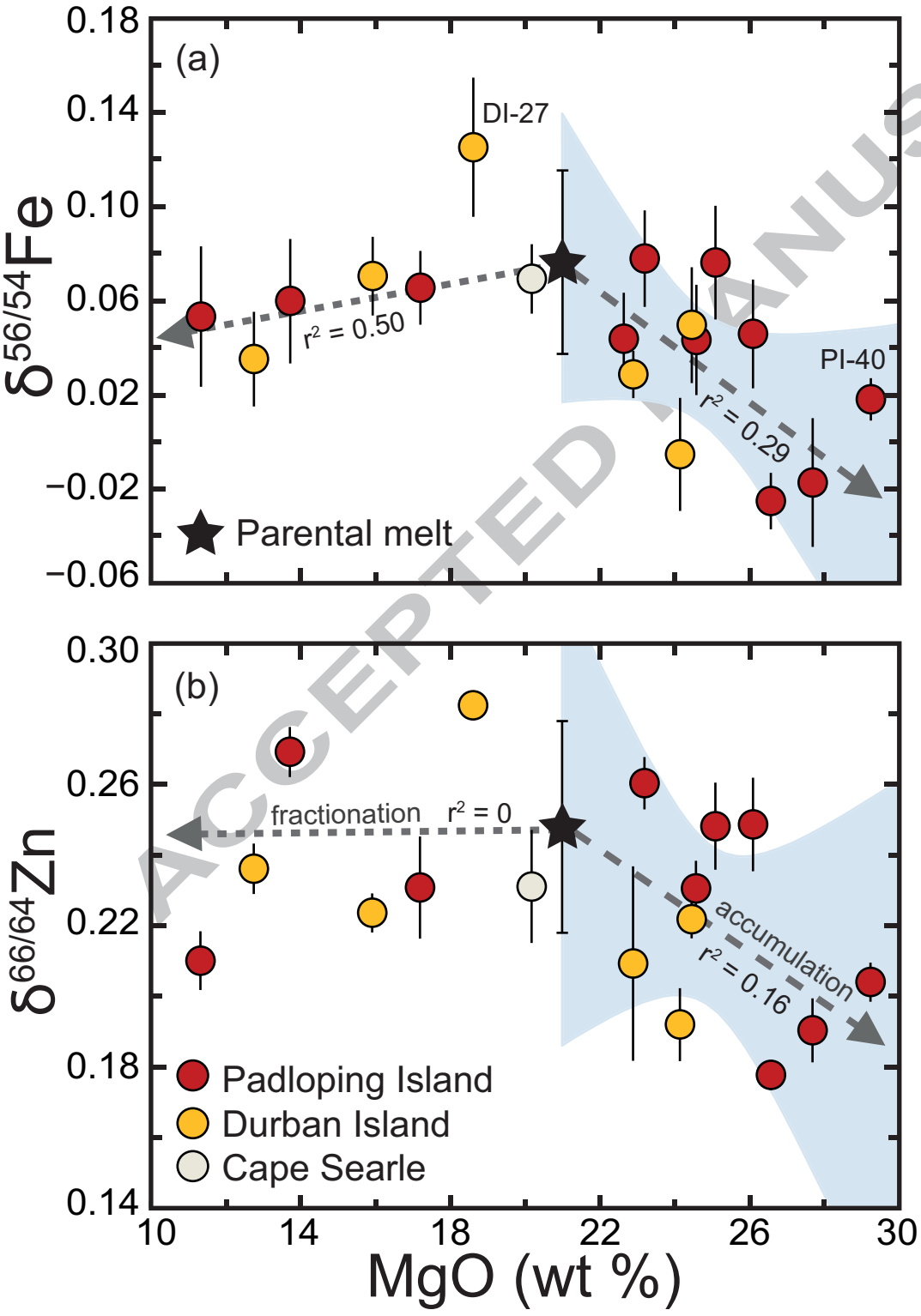

Figure 4

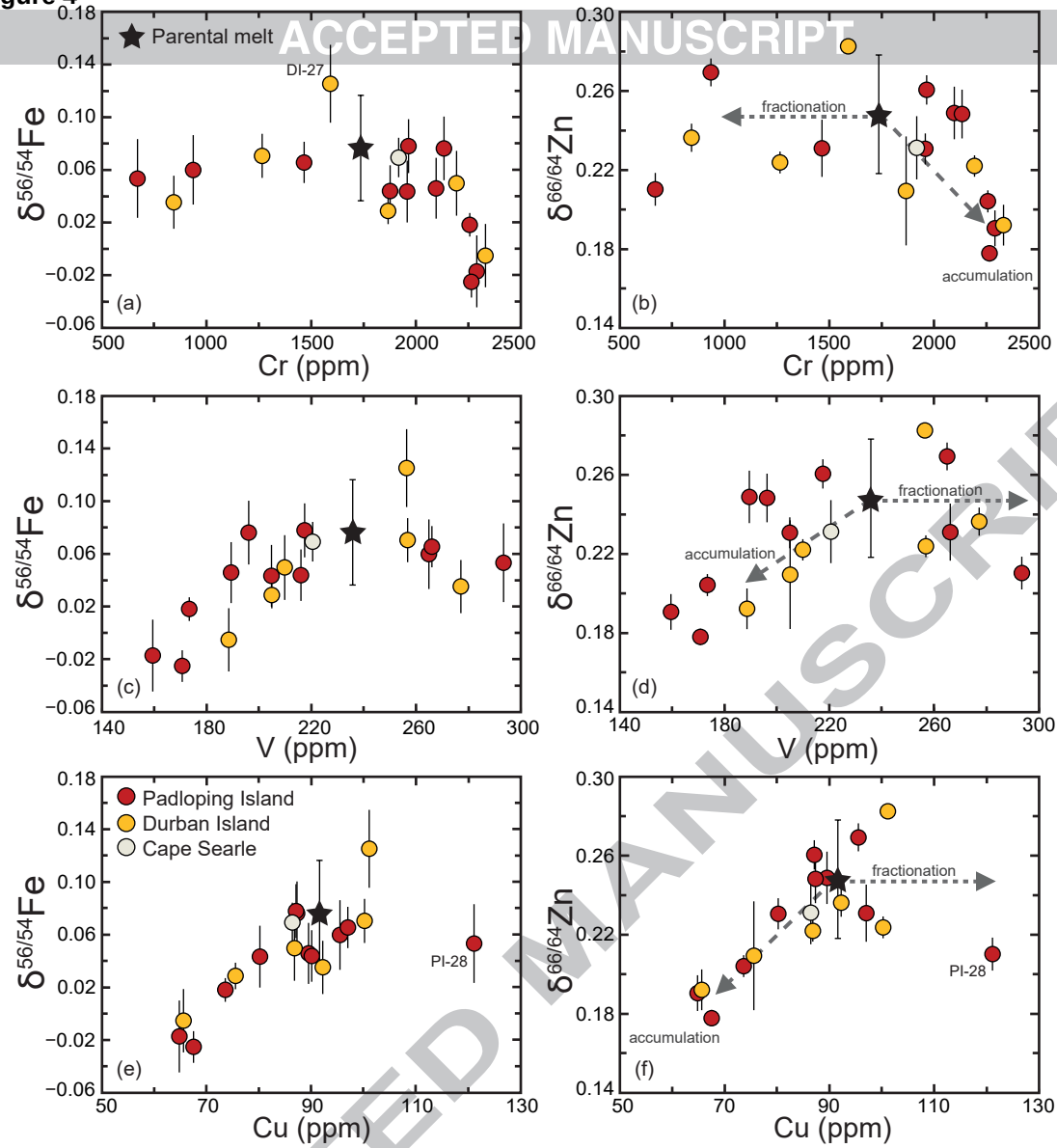

Figure 5

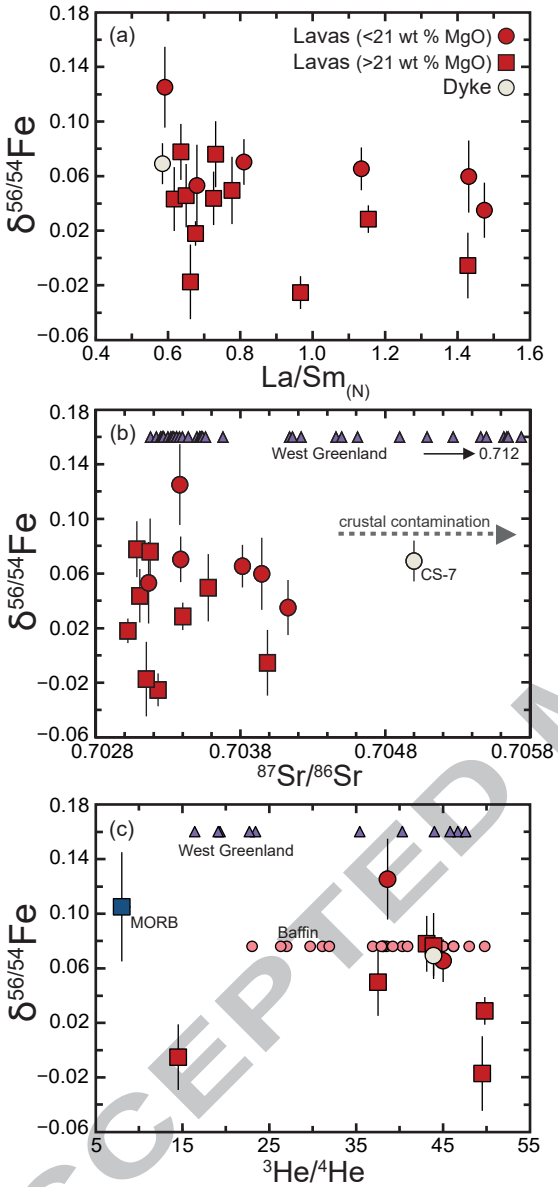

Figure 6

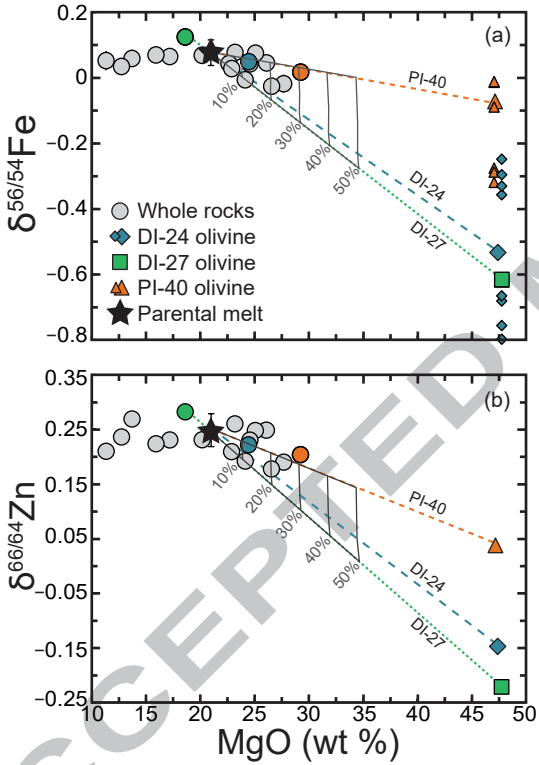

Figure 7

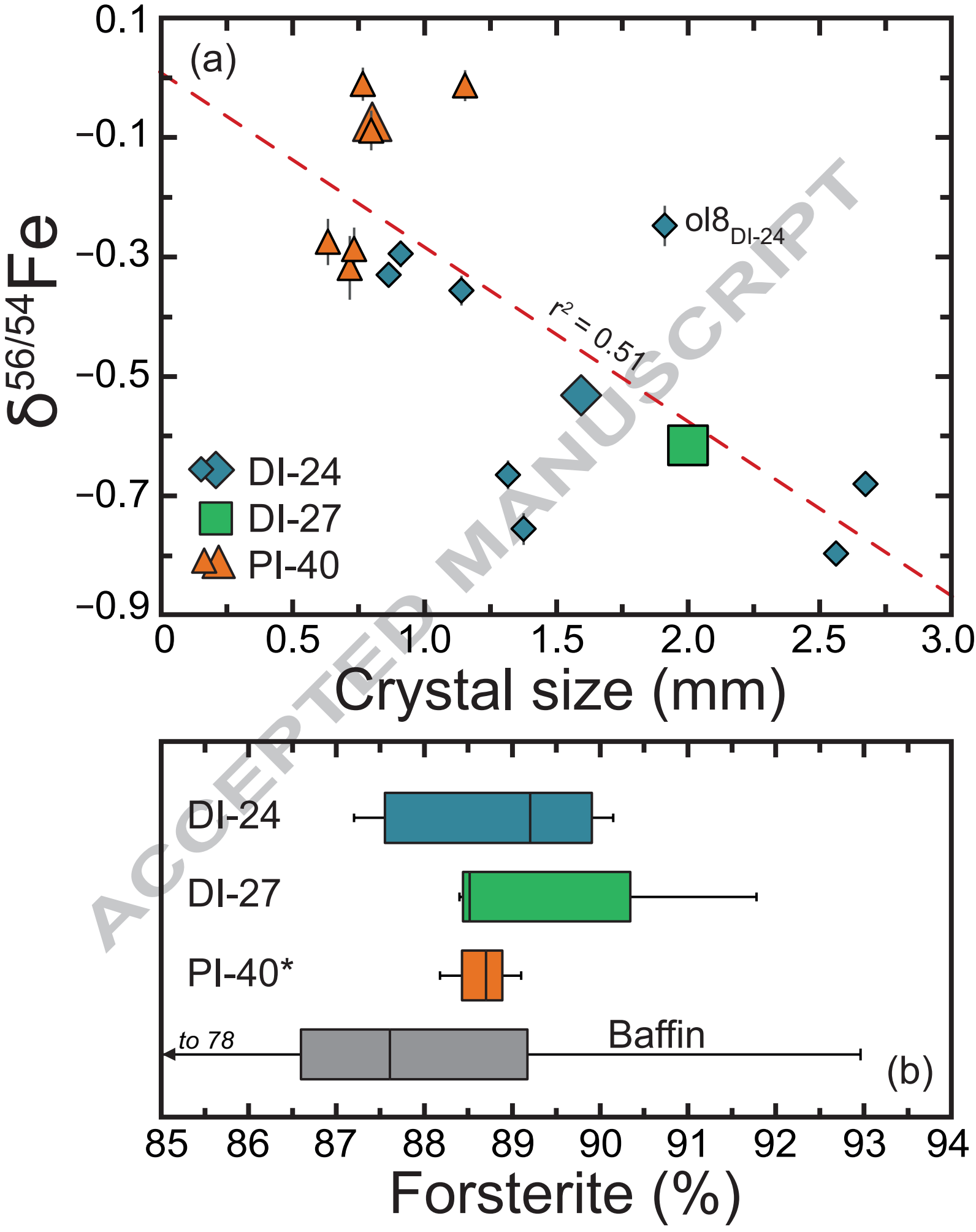

Figure 8

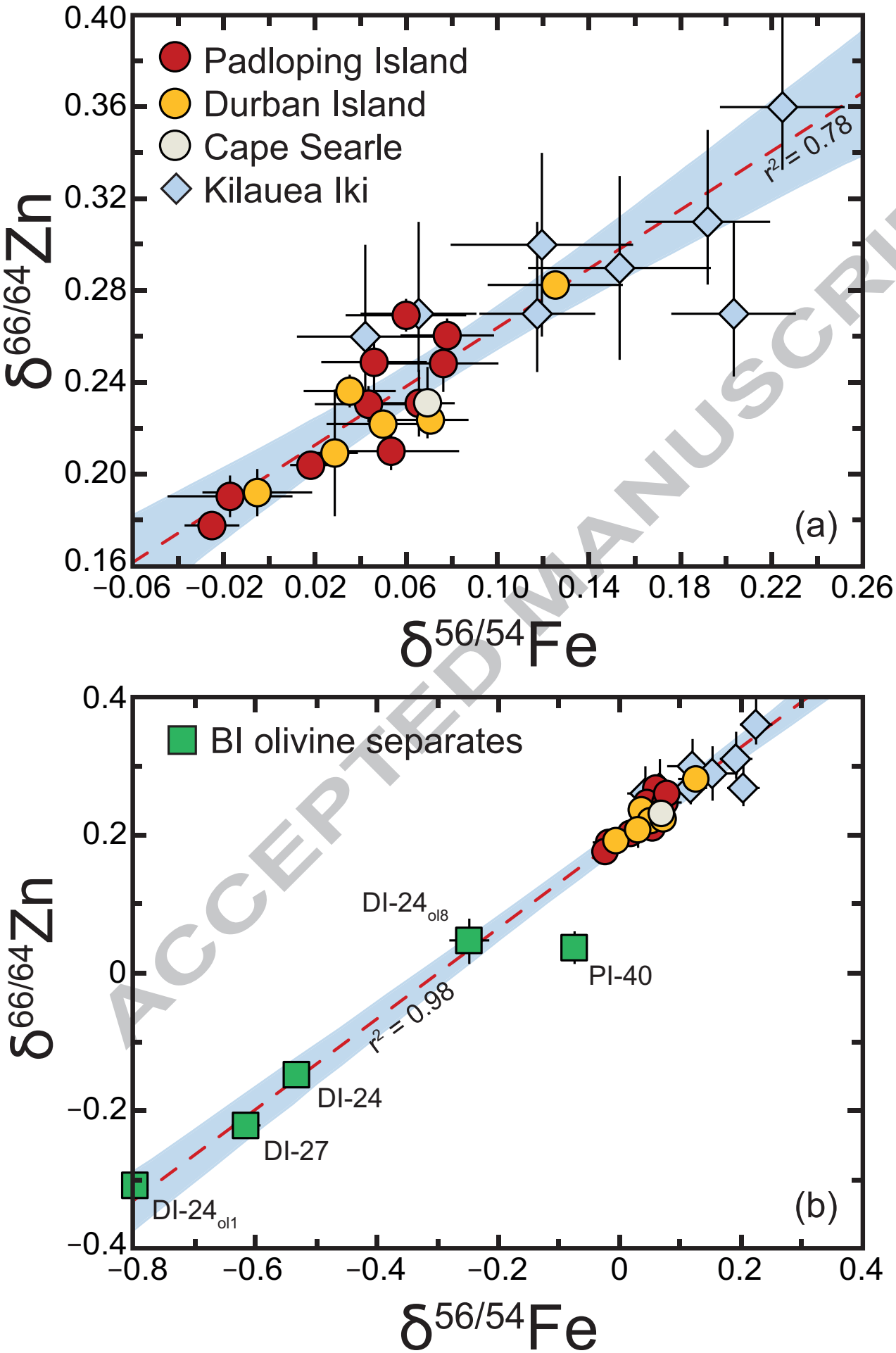

Figure 9

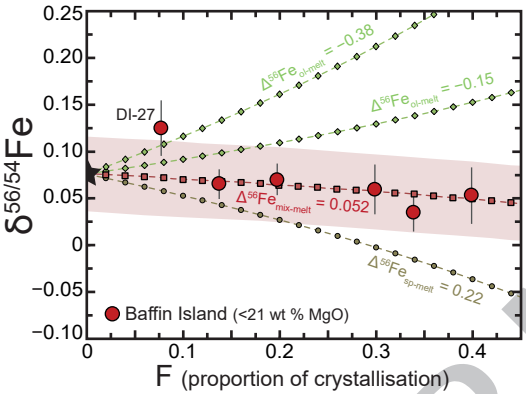

Figure 10

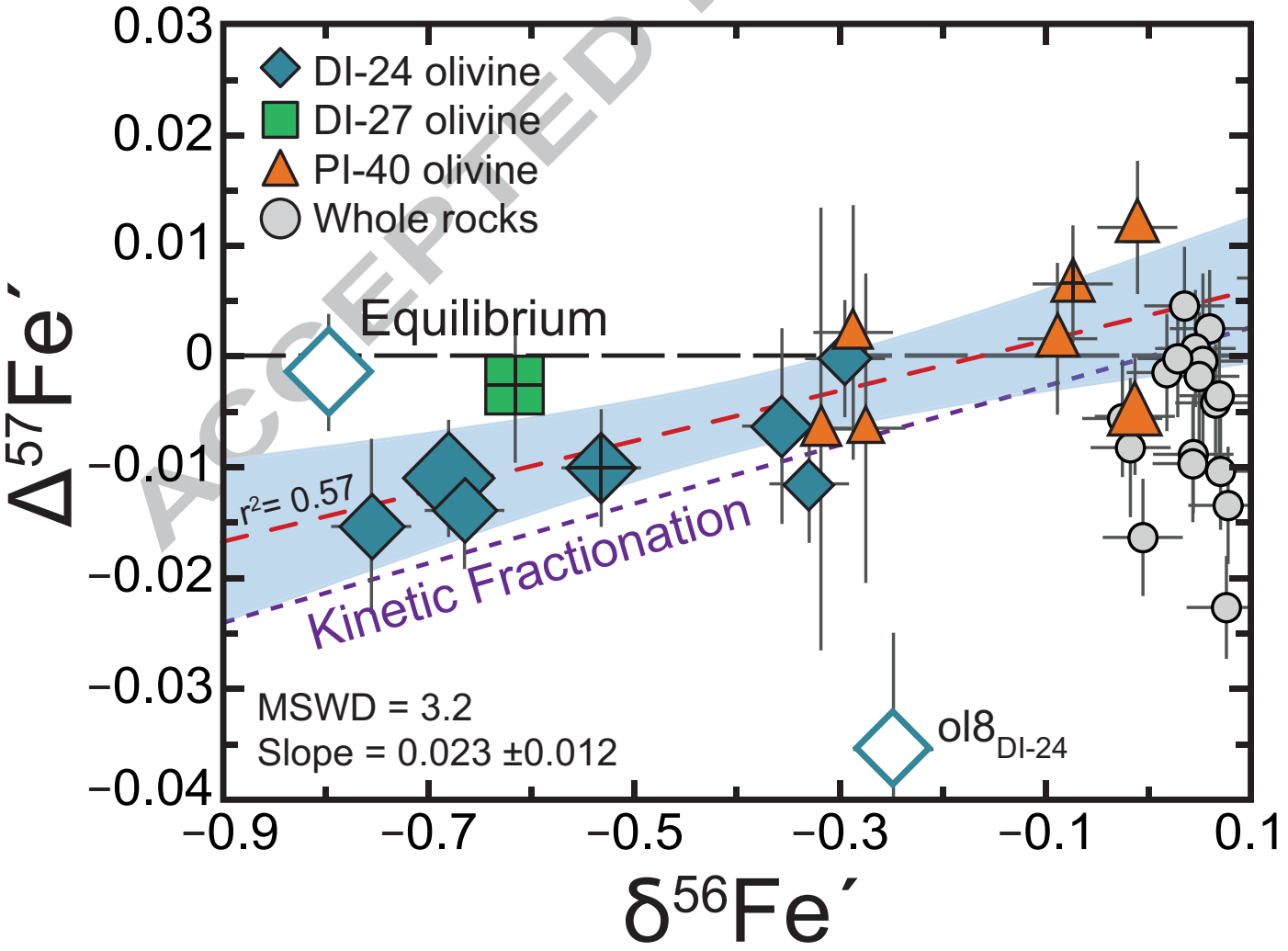

Figure 11

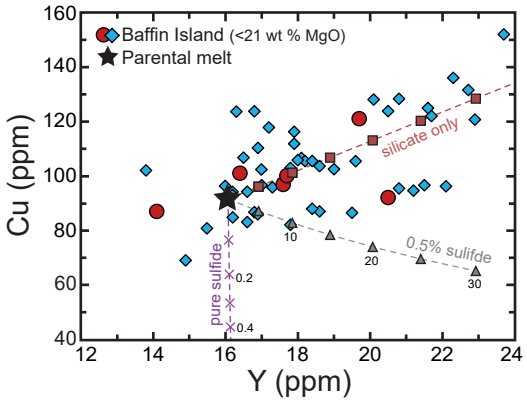

Figure 12

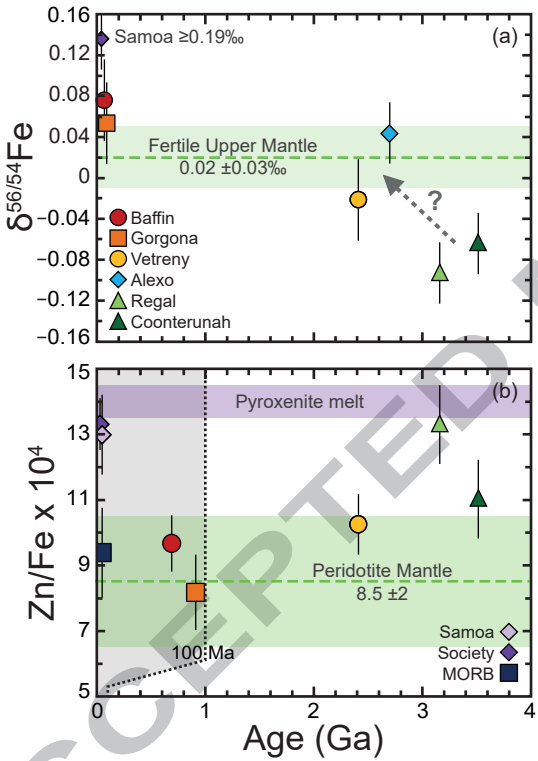

Figure 13

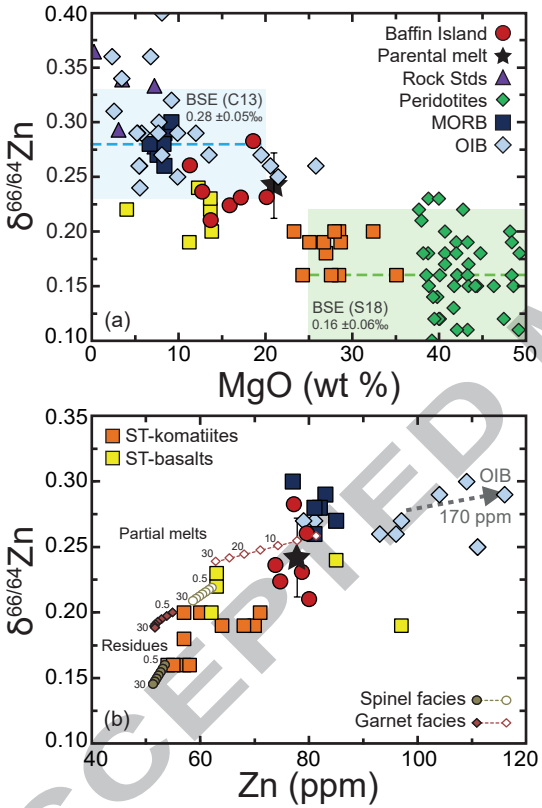

fractionation factor has been estimated assuming that light Zn isotopes partition into garnet analogous to Fe isotopes (An et al., 2017).

Table 1: The Fe and Zn isotope composition of Baffin Island picrites and selected rock standards

Sample	MgO (wt %)	Cu (ppm)	δ^{56}Fe (‰)	2 s.d.	95% s.e.	*n*	δ^{66}Zn (‰)	2 s.d.	95% s.e.	*n*
Baffin Island Samples										
Padloping Island										
PI-22	13.72	95.5	0.060	0.069	0.026	*9*	0.269	0.017	0.007	*8*
PI-24	26.10	89.5	0.046	0.065	0.023	*10*	0.262	0.017	0.008	*7*
PI-24 (2)							0.236	0.042	0.019	*7*
PI-24 Av.							0.249	0.041	0.013	*14(2)*
PI-25	27.69	64.8	−0.017	0.086	0.027	*12*	0.191	0.017	0.009	*6*
PI-26	25.09	87.3	0.076	0.058	0.024	*8*	0.262	0.021	0.010	*7*
PI-26 (2)							0.233	0.035	0.019	*6*
PI-26 Av.		87.1					0.248	0.041	0.012	*13(2)*
PI-27	23.20		0.069	0.082	0.027	*11*	0.274	0.022	0.010	*7*
PI-27 (2)			0.098	0.049	0.031	*5*	0.237	0.042	0.033	*4*
PI-27 Av.			0.078	0.077	0.020	*16(2)*	0.261	0.047	0.007	*11(2)*
PI-28	11.33	121.1	0.053	0.071	0.030	*8*	0.210	0.020	0.008	*8*
PI-31	22.64	90.1	0.044	0.047	0.020	*8*				
PI-37	26.57	67.5	−0.025	0.036	0.012	*11*	0.181	0.014	0.006	*7*
PI-37 (2)							0.174	0.045	0.023	*6*
PI-37 Av.							0.178	0.031	0.004	*13(2)*
PI-40	29.24	73.6	0.023	0.030	0.013	*8*	0.203	0.023	0.009	*8*
PI-40 (2)			0.013	0.034	0.016	*7*	0.205	0.020	0.008	*8*
PI-40 Av.			0.018	0.032	0.009	*15(2)*	0.204	0.021	0.006	*16(2)*
PI-43	24.58	80.2	0.043	0.056	0.023	*8*	0.231	0.013	0.008	*5*
PAD-6	17.20	97.0	0.065	0.034	0.016	*7*	0.231	0.028	0.014	*6*

Durban Island										
DI-22	12.75	92.2	0.035	0.044	0.020	*7*	0.236	0.017	0.007	*8*
DI-23	24.14	65.6	–0.005	0.058	0.024	*8*	0.192	0.020	0.010	*6*
DI-24	24.46	86.8	0.050	0.059	0.025	*8*	0.222	0.013	0.005	*8*
DI-26	15.92	100.2	0.070	0.040	0.017	*8*	0.235	0.018	0.008	*7*
DI-26 (2)							0.210	0.037	0.019	*6*
DI-26 Av.							0.224	0.037	0.006	*13(2)*
DI-27	18.62	101.1	0.125	0.071	0.030	*8*	0.283	0.008	0.003	*8*
DUR-8	22.89	75.5	0.029	0.016	0.010	*5*	0.209	0.052	0.028	*7*
Cape Searle										
CS-7	20.18	86.4	0.073	0.046	0.019	*8*	0.231	0.030	0.016	*6*
CS-7 (2)			0.063	0.056	0.035	*5*				
CS-7 Av.			0.069	0.049	0.015	*13(2)*				
<u>Rock Standards</u>										
AMH-1							0.243	0.025	0.011	*7*
BCR-2							0.234	0.018	0.009	*6*
BIR-1			0.052	0.050	0.019	*9*	0.237	0.013	0.005	*8*
BIR-1 (2)			0.054	0.031	0.012	*9*	0.257	0.031	0.013	*8*
BIR-1 (3)			0.055	0.039	0.024	*5*				
BIR-1 Av.			0.054	0.039	0.009	*23(3)*	0.247	0.030	0.008	*16(2)*
BHVO-2			0.095	0.029	0.015	*6*	0.307	0.016	0.005	*13*
DNC-1			0.066	0.021	0.010	*7*	0.242	0.029	0.013	*7*
RGM-1							0.353	0.025	0.013	*6*
<u>Mass Spectrometry Solutions</u>										
FeCl			–0.722	0.046	0.004	*130*				
JMC-Lyon							0.009	0.022	0.007	*19*

Table 2: The Fe and Zn isotope composition of bulk and individual olivine phenocrysts

Sample	Weight (mg)	Size[a] (mm)	δ^{56}Fe (‰)	2 s.d.	95% s.e.	*n*	δ^{66}Zn (‰)	2 s.d.	95% s.e.	*n*
DI-24_Bulk	41.3	1.59	−0.532	0.056	0.020	*10*	−0.147	0.026	0.012	*7*
DI-24 ol-1	9.17	2.56	−0.797	0.047	0.019	*8*	−0.308	0.015		*3*
DI-24 ol-2	1.70	1.38	−0.756	0.064	0.027	*8*				
DI-24 ol-3	4.76	2.67	−0.680	0.044	0.020	*7*				
DI-24 ol-4	0.86	1.14	−0.356	0.060	0.025	*8*				
DI-24 ol-5	0.90	0.91	−0.295	0.053	0.022	*8*				
DI-24 ol-6	0.60	1.32	−0.665	0.058	0.024	*8*				
DI-24 ol-7	0.36	0.86	−0.330	0.043	0.018	*8*				
DI-24 ol-8	4.44	1.91	−0.248	0.065	0.034	*6*	0.047	0.033		*2*
DI-27_Bulk	43.5	2.00	−0.616	0.064	0.023	*10*	−0.221	0.042	0.017	*8*
DI-27_Leach			−0.504	0.050	0.026	*6*				
PI-40_Bulk	39.5	0.80	-0.073	0.030	0.011	9	0.037	0.053	0.024	*7*
PI-40 ol-1	1.40	1.15	-0.013	0.061	0.026	8				
PI-40 ol-2	0.26	0.63	-0.275	0.074	0.039	6				
PI-40 ol-3	0.23	0.72	-0.318	0.086	0.053	5				
PI-40 ol-4	0.36	0.73	-0.287	0.079	0.036	7				
PI-40 ol-5	0.38	0.80	-0.088	0.053	0.033	5				
PI-40 ol-6	0.25	0.77	-0.011	0.045	0.028	5				

Table 3: Age, MgO contents and Fe isotopes compositions and Zn/Fe ratios of mantle melts.

Location	Age (Ga)	MgO (wt %)[a]	δ^{56}Fe (‰)[b]	Zn/Fe x 10^{4}[c]
High degree partial melts				
Baffin Island	0.069	21	0.076 ± 0.04	9.67 ± 0.86
Gorgona	0.091	23	0.054 ± 0.04	8.18 ± 1.15
Vetrney	2.41	18	−0.021 ± 0.04	10.25 ± 0.92
Alexo	2.7	29.1	0.044 ± 0.03	--
Regal	3.16	29	−0.093 ± 0.03	13.29 ± 1.2
Coonterunah	3.515	23	−0.064 ± 0.03	11.02 ± 1.2
Ocean Island Basalts				
Samoa	<0.005		≥0.19	12.99 ± 1.22
Society Islands	<0.003	10	0.136 ± 0.03	13.31 ± 0.79
MORB			0.105 ± 0.04	9.39 ± 1.37
Peridotite Mantle[d]			0.033 ± 0.04	8.50 ± 2.0

Table 4: Model parameters for the calculation of Zn isotope fractionation during non-modal fractional melting in the garnet facies mantle.

Phase	Starting fraction[a]	Melting reaction[a]	Partitioning	D_{Zn}[b]	$\Delta^{66}Zn$ (‰)[c]
Olivine	0.52	0.08	ol-melt	0.96	$-0.17 \times 10^6/T^2$
Orthopyroxene	0.22	−0.19	opx-melt	0.451	$-0.17 \times 10^6/T^2$
Clinopyroxene	0.16	0.81	cpx-melt	0.333	$-0.17 \times 10^6/T^2$
Garnet	0.1	0.30	grt-melt	0.213	$-0.20 \times 10^6/T^2$
			mantle-melt	0.67	$-0.178 \times 10^6/T^2$